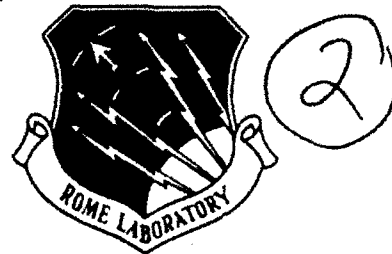
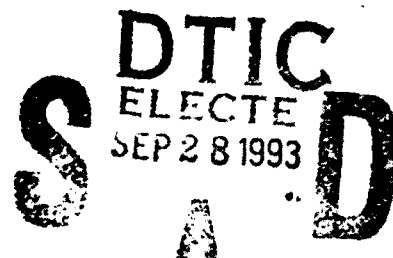


RL-TR-92-333  
In-House Report  
December 1992

AD-A270 004



# DESIGN AND FABRICATION OF A MULTICHANNEL ADAPTIVE OPTICAL PROCESSOR (MADOP)



Michael J. Ward, Capt, USAF; Christopher W. Keefer, Capt,  
USAF; Harold G. Andrews II, 1Lt, USAF

*APPROVED FOR PUBLIC RELEASE; DISTRIBUTION UNLIMITED.*

93-22412



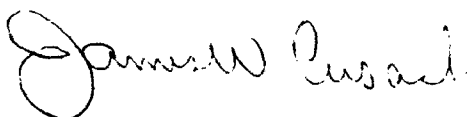
Rome Laboratory  
Air Force Materiel Command  
Griffiss Air Force Base, New York

93 9 27 0 1 7

This report has been reviewed by the Rome Laboratory Public Affairs Office (PA) and is releasable to the National Technical Information Service (NTIS). At NTIS it will be releasable to the general public, including foreign nations.

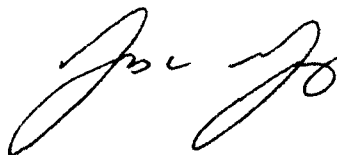
RL-TR-92-333 has been reviewed and is approved for publication.

APPROVED:



JAMES W. CUSACK, Chief  
Photonics & Optics Division  
Surveillance and Photonics Directorate

FOR THE COMMANDER:



JAMES W. YOUNGBERG, LtCol, USAF  
Deputy Director  
Surveillance and Photonics Directorate

If your address has changed or if you wish to be removed from the Rome Laboratory mailing list, or if the addressee is no longer employed by your organization, please notify RL (OCPA) Griffiss AFB NY 13441-5700. This will assist us in maintaining a current mailing list.

Do not return copies of this report unless contractual obligations or notices on a specific document require that it be returned.

# REPORT DOCUMENTATION PAGE

Form Approved  
OMB No. 0704-0188

Public reporting burden for this collection of information is estimated to average 1 hour per response, including the time for reviewing instructions, searching existing data sources, gathering and maintaining the data needed, and completing and reviewing the collection of information. Send comments regarding this burden estimate or any other aspect of this collection of information, including suggestions for reducing this burden, to Washington Headquarters Services, Directorate for Information Operations and Reports, 1215 Jefferson Davis Highway, Suite 1204, Arlington, VA 22202-4302, and to the Office of Management and Budget, Paperwork Reduction Project (0704-0188), Washington, DC 20503.

1. AGENCY USE ONLY (Leave Blank)		2. REPORT DATE December 1992		3. REPORT TYPE AND DATES COVERED In-House Feb 91 - Sep 92	
4. TITLE AND SUBTITLE DESIGN AND FABRICATION OF A MULTICHANNEL ADAPTIVE OPTICAL PROCESSOR (MADOP)				5. FUNDING NUMBERS PE - 62702F PR - 4600 TA - P1 WU - 07	
6. AUTHOR(S) Michael J. Ward, Capt, USAF; Christopher W. Keefer, Capt, USAF; Harold G. Andrews II, 1Lt, USAF					
7. PERFORMING ORGANIZATION NAME(S) AND ADDRESS(ES) Rome Laboratory (OCPA) 25 Electronic Parkway Griffiss AFB NY 13441-4515				8. PERFORMING ORGANIZATION REPORT NUMBER RL-TR-92-333	
9. SPONSORING/MONITORING AGENCY NAME(S) AND ADDRESS(ES) Rome Laboratory (OCPA) 25 Electronic Parkway Griffiss AFB NY 13441-4515				10. SPONSORING/MONITORING AGENCY REPORT NUMBER	
11. SUPPLEMENTARY NOTES Rome Laboratory Project Engineer: Michael J. Ward, Capt, USAF/OCPA (315) 330-2944					
12a. DISTRIBUTION/AVAILABILITY STATEMENT Approved for public release; distribution unlimited.				12b. DISTRIBUTION CODE	
13. ABSTRACT (Maximum 200 words) We designed and built a multichannel adaptive optical processor (MADOP) for the purpose of adaptive cancellation of broadband jamming noise in C-Band antenna arrays. The processor operates at an intermediate frequency (IF) of 80 MHz and is designed to provide greater than 30 dB cancellation of two independent 10 MHz bandwidth noise jammers, where multiple reflections of the jamming energy collected in the sidelobes produce multipath delays of up to 5 usec. The MADOP architecture is portable and designed to function as an on-line "smart filter" which adaptively cancels broadband noise in the sidelobes.					
14. SUBJECT TERMS optical signal processing, adaptive processing, acousto-optics, noise cancellation				15. NUMBER OF PAGES 64	
				16. PRICE CODE	
17. SECURITY CLASSIFICATION OF REPORT UNCLASSIFIED		18. SECURITY CLASSIFICATION OF THIS PAGE UNCLASSIFIED		19. SECURITY CLASSIFICATION OF ABSTRACT UNCLASSIFIED	
				20. LIMITATION OF ABSTRACT U/L	

## Contents

Accession For		
NTIS	CRA&I	<input checked="" type="checkbox"/>
DTIC	TAB	<input type="checkbox"/>
Unannounced		<input type="checkbox"/>
Justification		
By		
Distribution/		
Availability Codes		
Dist	Avail and/or Special	
A-1		

List of Figures  
Acknowledgements

DTIC QUALITY INSPECTED 3

1. Introduction
  - 1.1 Requirements
  - 1.2 Overview of In-House Plan
  - 1.3 Organization of Paper
2. Application of Adaptive Cancellation to Jamming Cancellation
  - 2.1 Radar Signal Processing Scenario
  - 2.2 Application of the Block Least Mean Squares Algorithm
  - 2.3 Simulated Block LMS Performance
3. Design Considerations
  - 3.1 Overall Considerations
  - 3.2 In-Line vs Mach-Zehnder Time Integrating Correlator
    - 3.2.1 In-Line Correlator
    - 3.2.2 Mach-Zehnder Interferometric Correlator
  - 3.3 Acousto-Optic Tapped Delay Line Alternatives
    - 3.3.1 Use of Acousto-Optic Spatial Light Modulator
      - 3.3.1.1 Selection of Components for Delay Line
      - 3.3.1.2 AOSLM Signal Generation Requirements
    - 3.3.2 Use of Laser Diode Array
  - 3.4 Different Interface Techniques
    - 3.4.1 All-Optical Interface
    - 3.4.2 Computer Controlled Interface
    - 3.4.3 Custom Electronic Interface
  - 3.5 Use of Neural Network Algorithm for Tap Selection
4. Fabrication and Testing of the MADOP Subsystems
  - 4.1 Multichannel Time Integrating Correlator
    - 4.1.1 Hardware Description
    - 4.1.2 Test Results
      - 4.1.2.1 Autocorrelation of Wideband Test Signals
      - 4.1.2.2 Autocorrelation w/ Delay and Multichannel Operation
  - 4.2 Multichannel Tapped Delay Line
    - 4.2.1 Hardware Description
    - 4.2.2 Test Results
  - 4.3 CCD Cameras, Computer Interface, and Controlling Software

- 4.3.1 Hardware Description
- 4.3.2 Computer Software Description
- 4.3.3 Test Results for Software Based Signal Processing
  - 4.3.3.1 Software Preprocessing
  - 4.3.3.2 Correlation Peak Determination
- 4.3.4 Future Enhancements

## 5. Conclusions and Recommendations

- 5.1 Recommendations for Time Integrating Correlator
- 5.2 Recommendations for Computer Interface
- 5.3 Recommendations for AO Tapped Delay Line
- 5.4 Concluding Remarks

## 6. References

## List of Figures

- 2.1.a Radar Signal Processing Scenario.
- 2.1.b MADOP Within Radar System.
  
- 3.2.1.a In-Line Time Integrating Correlator.
- 3.2.1.b RF Input Spectrum to AO Device for In-Line System.
  
- 3.2.2.a Mach-Zehnder Interferometric Time Integrating Correlator.
- 3.2.2.b Conceptual Diagram of Autocorrelation with Mach-Zehnder Interferometric Time Integrating Correlator.
  
- 3.3.1.a Acousto-Optic Spatial Light Modulator Used to Tap Acousto-Optic Delay Line.
  - 3.3.1.1.a Bandwidth of AOSLM Sets Angular Deflection Range,  $\theta_{\max} - \theta_{\min}$ , and the Scan Range,  $\delta_{\text{scan}}$ .
  - 3.3.1.1.b Two Optical Taps Addressing AO Delay Line.
  - 3.3.1.1.c Size of Overlap Between Undiffracted and Diffracted Beams at the Photodiode.
  
  - 3.3.1.2.a Signal Generation Scheme for AOSLM Driving Signals With Four Output Weights.
  
- 3.3.2.a Programmable Laser Diode Array Forming Optical Taps onto AO Delay Line.
  - 3.3.2.b Proof-of-Concept Demonstration of Using a Programmable Tapped Delay Line Using a Laser Diode Array.
  - 3.3.2.c Geometry of Sharply Focused Optical Tap.
  - 3.3.2.d Oscilloscope Trace of Time Delay Generated for Four Unique Tap Positions.
  - 3.3.2.e Amplitude Response of Heterodyne Detected Pulses as a Function of Tap Position.
  
- 3.4.3.a Analog Circuit to Control Laser Diode Array with Photodiode Array Output.
  
- 4.1.2.1.a Oscilloscope Trace of Pulsed Input, 1 $\mu$ sec Pulsewidth, on 80 MHz Carrier.
- 4.1.2.1.b RF Spectrum of Pulsed Input.
- 4.1.2.1.c Optically Computed Autocorrelation of 100 nsec Pulse on 80 MHz

Carrier.

**4.1.2.1.d** Optically Computed Autocorrelation of 500 nsec Pulse on 80 MHz Carrier.

**4.1.2.1.e** Optically Computed Autocorrelation of 1000 nsec Pulse on 80 MHz Carrier.

**4.1.2.1.f** RF Spectrum of Broadband Noise Signal.

**4.1.2.1.g** Optically Computed Autocorrelation of a 10 MHz Noise Source.

**4.1.2.2.a** Signal Generation Scheme for Multichannel Autocorrelation of 10 MHz Noise Signals.

**4.1.2.2.b** Multichannel Autocorrelation of Delayed 10 MHz Noise Signals.

**4.2.2.a** Frequency Response of AO Tapped Delay Line as a Function of Tap Position.

**4.2.2.b** Frequency Response of a Fixed Tap Position Corresponding to an AOSLM Input Frequency of 76 MHz.

**4.2.2.c** Cancellation of Pulsed RF Input (100 nsec pulse width, 3  $\mu$ sec repetition) with a Single Tap.

**4.2.2.d** Cancellation of Pulsed RF Input (500 nsec pulse width, 3  $\mu$ sec repetition) with a Single Tap.

**4.3.1.a** Computer Controlled Interface.

**4.3.3.1.a-d** Preprocessing of Autocorrelation Data of 10 MHz Noise Source

**4.3.3.1.e** Spatial Carrier Prior to Amplitude Unification.

**4.3.3.1.f** Spatial Carrier After Amplitude Unification.

**4.3.3.1.g** Effects of Spatial Carrier Unification on the Correlation of Wide Bandwidth Noise.

## Acknowledgements

The in-house MADOP team recognizes the important contributions of the Dynetics staff: Dr. Merv Budge, Mr. Robert Berinato, and Mr. Michael Zari; and of Dr. Stephen Welstead of COLSA, Inc. Further thanks are due to Mr. David Gruzca who has provided key insights and assistance throughout the program and to Mr. Paul Payson for his work in generating test signals.



## 1. Introduction

**1.1 Requirements.** The Air Force needs an efficient processing system which can adaptively cancel multisource multipath jamming noise. Jamming energy directionally coupled into the sidelobes of an antenna gain pattern may consist of direct path noise as well as multipath from several independent jamming sources. This noise may limit or negate the effectiveness of Air Force surveillance and communications systems. Because of practical limitations (eg., speed, size, inability to perform parallel processing) existing digital sidelobe cancelers inadequately address this problem. Digital sidelobe cancelers require a separate processing channel for every multipath from every jammer. Each processing channel must include a discretely tapped RF delay line of length equal to or greater than the maximum multipath delay expected.

This report describes the design considerations for an acousto-optic (AO) based signal processor which is well suited for this application. A single AO time integrating correlator could replace whole racks of digital equipment in computing the correlation of the wide bandwidth signals received by the antennas. Furthermore, an acousto-optic based RF delay line provides long delays and extremely fine tap resolutions unmatched by any digital technology. The adaptive processing system described here uses both the AO correlator and the AO delay line circuits to perform massively parallel computations which are unique to the realm of optical processing. We believe the AO based adaptive processor, which was designed to the system requirements of a C-band antenna array, represents a solid solution to the problem of multisource multipath jamming noise.

System design requirements were defined by the operators of the Rome Laboratory C-Band Antenna array located at Griffiss Air Force Base, NY. They expressed a need for a multichannel adaptive processor which would satisfy the design requirements listed in Table I. Specifically, the MADOP was built to provide adaptive cancellation of broadband (<10 MHz) noise at the system intermediate frequency (IF) of 80 MHz. The processor is designed to provide 30 dB cancellation of up to two independent noise jammers, where multiple reflections of the jamming energy produce multipath delays of up to 5  $\mu$ sec.

We implemented a three phase in-house effort (described in Section 1.2) to provide a portable multichannel adaptive optical processor (MADOP) testbed. This report explains Phase II of this effort, the design and fabrication of the MADOP testbed.

Table I: Short and Long Term Design Requirements

Requirements	Long Term Goals	Short term Goals
Cancellation Ratio	40 dB	30 dB
Number of Jammers	4	2
Multipath Delay	20 $\mu$ sec	5 $\mu$ sec
Loop-Lock Time	5 msec	500 msec
System Bandwidth	10 MHz	10 MHz
Number of Multipath Delays	>4	2

**1.2 Overview of In-House Plan.** The MADOP in-house effort, which began in October, 1988, consists of three project phases. During Phase I (JON 4600P103) we explored the optical implementation of the LMS algorithm, and we designed, built, and tested a single channel adaptive optical processor for narrowband signals.<sup>1</sup> Characterization and testing of various spatial light modulation (SLM) techniques for forming the optical taps on the AO tapped delay line proved to be an important aspect of this effort.<sup>2,3,4,5</sup> One result of this research was a patented SLM technique, "Extended Dynamic Range One Dimensional Spatial Light Modulator."<sup>6</sup> The in-house team consisted of Capt. Michael Ward and Capt. Christopher Keefer. The in-house effort was supported by two Expert in Science and Engineering (ESE) contracts, "Hybrid Electro-Optical Processor"<sup>7</sup> (F30602-88-D-0027) and "Optical Processor Evaluation"<sup>8</sup> (F30602-88-D-0028). Both contracts were performed by Dr. Stephen Welstead of COLSA, Inc., Huntsville, AL.

Phase II (JON 4600P107) applied the results of the single channel optical processor to the design and fabrication of a two channel adaptive optical processor and is the subject of this final report. We examined alternative algorithms, including neural networks<sup>9</sup>, during the course of this effort in an attempt to offset the limitations of the SLM technology. Different architectures for both the AO time integrating correlator and AO tapped delay line were considered, built, and compared. The resulting system shows promise for success in Phase III. The in-house team consisted of Capt. Michael Ward, Capt. Christopher Keefer, and 1Lt Harold Andrews II. The in-house effort was supported by two ESE contracts, "Algorithms for Multichannel Optical Processor"<sup>10</sup> (F30602-88-D-0028), performed by Dr. Stephen Welstead of COLSA, and "Acousto-optic Applications to Multichannel Optical Processor"<sup>11</sup> (F30602-91-D-0001), performed by Dr. Merv Budge, Mr. Robert Berinato, and Mr. Michael Zari of Dynetics, Inc., Huntsville, AL. The Dynetics staff also

provided support in an FY92 effort entitled, "Alternative Acousto-optic Architectures for Multichannel Adaptive Optical Processor,"<sup>12</sup> (F30602-92-C-0026) in response to a Broad Agency Announcement (90-04).

Phase III (JON 4600P114) will conduct extensive test and evaluation of the MADOP system built in Phase II. These tests will include some "on-line" time with the C-Band antenna and may result in design modifications. At the end of Phase III, we hope to deliver a fully tested two channel adaptive optical processor in response to the near term requirements listed in Table I. This breadboard system will serve as a practical demonstration of the computing power of optical processors applied to adaptive jamming cancellation.

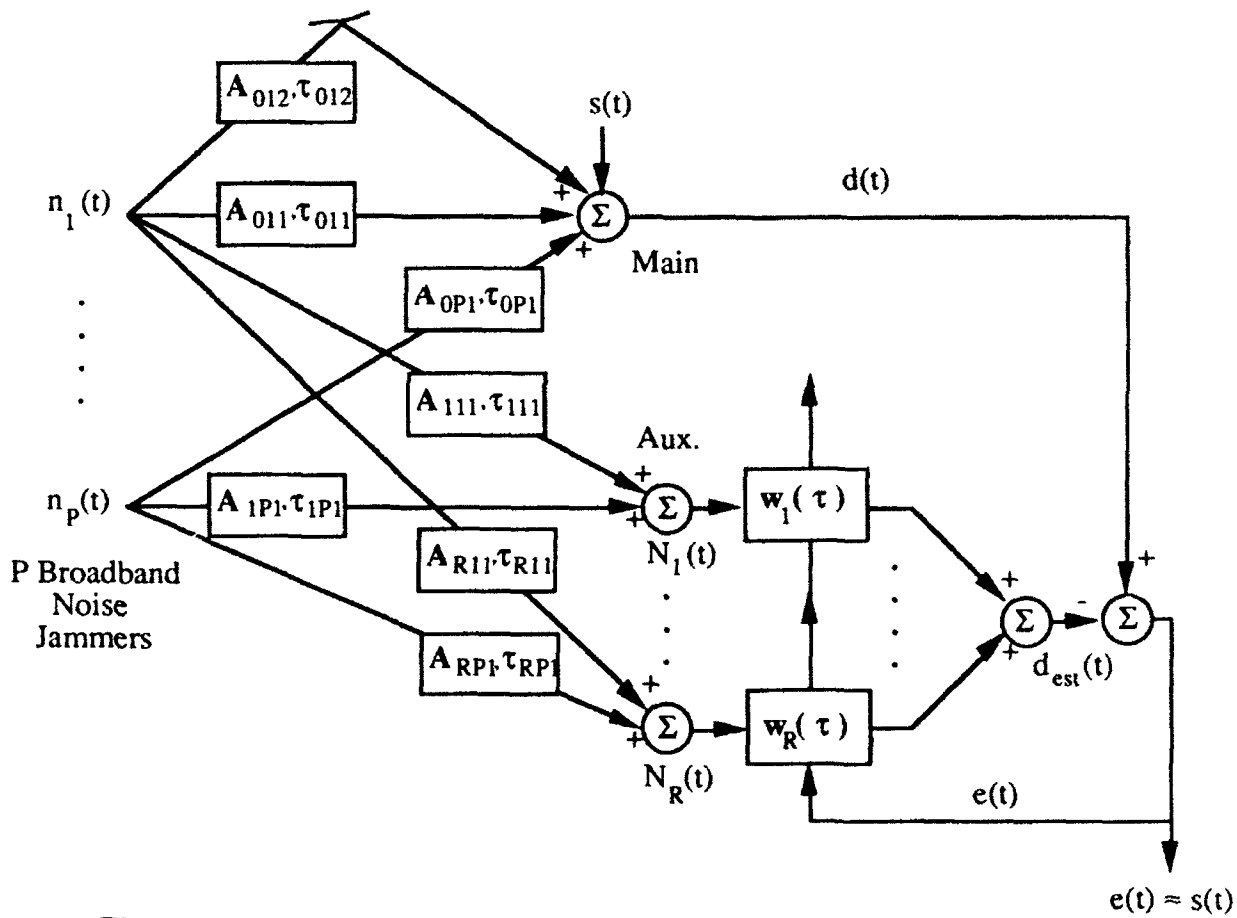


**Figure 2.1.a Radar Signal Processing Scenario.** Antenna array with one main antenna and R auxiliary antennas receives signal of interest,  $s(t)$ , in the presence of P broadband noise jammers. Although many multipaths may occur, only one multipath (from jammer 1 into main antenna) is shown for simplicity. An adaptive weight vector is formed for each auxiliary channel as described in Section 2.2. The vector sum forms an estimate to the composite multipath jamming signal present in the main channel.

**1.3 Organization of Report.** In Section 2, the report reviews the radar signal processing scenario and describes the Block-LMS algorithm implemented by the MADOP architecture. Section 3 discusses several of the key issues which affected the design process. Section 4 explains each of the subsystems and presents some preliminary test data. We close the report in Section 5 with recommendations and conclusions.

## 2. Application of Adaptive Processing to Jamming Cancellation

**2.1 Radar Signal Processing Scenario.** Consider an antenna array with one directional main antenna and R omni-directional auxiliary antennas. Figure 2.1.a depicts such an array attempting to detect a target return signal,  $s(t)$ , in the presence of P broadband noise jammers, where  $P \leq R$ .

The main antenna receives  $s(t)$  into the main receiving lobe and a compilation of noise signals and multipath reflections of noise signals coupled into the sidelobes. Thus the composite signal received by the main antenna,  $d(t)$ , for the case  $P=2$  may be expressed as

$$d(t) = s(t) + \sum_{m=1}^{M_{01}} A_{01m} \cdot n_1(t-\tau_{01m}) + \sum_{m=1}^{M_{02}} A_{02m} \cdot n_2(t-\tau_{02m}) \quad (2.1.1)$$

where  $n_p(t)$ , for all  $1 \leq p \leq P$ , is the noise signal from the  $p$ th jamming source.  $M_{0p}$  represents the total number of multipath reflections from the  $p$ th jammer received by the main antenna. The  $A_{0pm}$ , for all  $1 \leq m \leq M_{0p}$ , represent the received gain of the  $m$ th multipath reflection from the  $p$ th jamming source into the main antenna, and are a function of the amplitude of the reflection and the sidelobe gain. The multipath delays,  $\tau_{0pm}$ , represent the time delay of the  $m$ th multipath reflection from the  $p$ th jamming source in travelling to the main antenna.

Likewise, each of the R auxiliary antennas receives a composite noise signal,  $N_r(t)$ , for all  $1 \leq r \leq R$ . Note that the  $r=0$  case represents the main antenna. The composite noise signal for the  $r$ th auxiliary can be expressed as

$$N_r(t) = \sum_{p=1}^P \sum_{m=1}^{M_{rp}} A_{rpm} \cdot n_p(t-\tau_{rpm}) \quad (2.1.2)$$

in which  $M_{rp}$  represents the total number of multipath reflections from the  $p$ th jammer into the  $r$ th antenna element. Also, the  $A_{rpm}$  represent the received gain of the  $m$ th multipath reflection from the  $p$ th jamming source into the  $r$ th antenna

element, and are a function of the multipath amplitude and antenna gain. The multipath delays,  $\tau_{pm}$ , are defined similarly.

The output from the main antenna and each of the auxiliary antennas is mixed down to a system intermediate frequency (IF), as shown in Figure 2.1.b. Digital post processing systems require a low noise signal,  $s(t)$ , in order to accurately detect and identify the target. However, the noise term present in Equation 2.1.1 masks the target return.

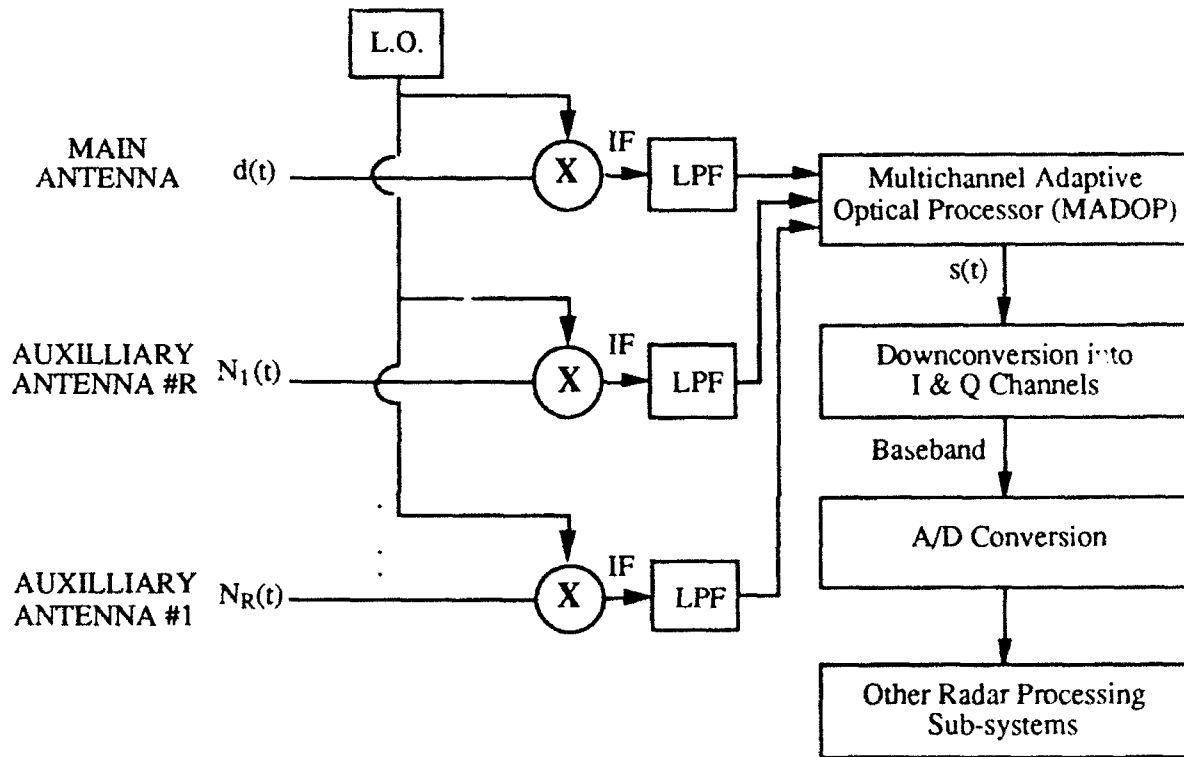


**Figure 2.1.b MADOP Within Radar System.** The MADOP receives signal inputs at the system IF from the main antenna and each of the auxiliary antennas. After performing its adaptive cancellation task, the MADOP suppresses the noise and extracts the target signal,  $s(t)$ , to be used in other signal processing tasks.

Our task is to build an optically based IF filter to cancel the noise term without suppressing  $s(t)$ . Assuming that the target return,  $s(t)$ , is of negligible amplitude relative to the noise amplitudes at each of the auxiliary antennas, this problem calls for an application of an adaptive algorithm such as least mean squares (LMS). The LMS algorithm makes use of the auxiliary antenna inputs in forming an estimate to the noise term in  $d(t)$ , as will now be explained in detail.

**2.2 Application of the LMS Algorithm** Widrow and Stearns described<sup>13</sup> applications of the LMS algorithm to such problems as extracting a fetal heartbeat from the mother's heartbeat, or cancelling surface acoustic noise from a geologic sensor. Our RF application falls in the same category of adaptive noise cancellation. When fed a main signal  $d(t)$  (consisting of a target return and noise), and a reference signal  $N_r(t)$  (containing correlated and possibly delayed versions of the noise), the LMS algorithm uses a weight vector  $w_r(\tau)$  to tap a delay line containing the  $r$ th reference signal. The output from the tapped delay line forms the noise signal estimate,  $y(t)$ . The estimate is subtracted from  $d(t)$ , forming an error signal,  $e(t)$ . The LMS algorithm steps along the error surface to a point where the mean square error (MSE) is minimized, ie. where the estimate most closely resembles the noise present in  $d(t)$ .

The weight vector is computed with each iteration according to the equation

$$w_{r(q)}(\tau) = \mu \cdot (-\Delta w_{r(q)}(\tau)) \quad (2.2.1)$$

where  $\mu$  represents the step size, and  $\Delta w_{r(q)}(\tau)$ , the weight vector update for the  $r$ th reference channel, approximates the gradient function of the error surface at  $\tau$  on the  $q$ th iteration. The weight vector update is computed by correlating the error signal,  $e(t)$ , with the reference noise signal,  $N_r(t)$ .

In the classical LMS algorithm, only the instantaneous correlation values are employed. However, in this application the weight vector is described by

$$w_{r(q)}(\tau) = w_{r(q-1)}(\tau) + \mu \cdot (-\Delta w_{r(q)}(\tau)) \quad (2.2.2)$$

where  $w_{r(q)}(\tau)$  now includes an accumulation of the previously calculated correlations, contained in the term  $w_{r(q-1)}(\tau)$ . This corresponds to the steepest descent algorithm, a subset of LMS. However, contrary to the LMS and steepest descent algorithms, in our system,  $w_{r(q)}(\tau)$  remains constant while  $\Delta w_{r(q)}(t)$  is being computed. The digital filtering community terms this approach "block-LMS." Its advantage over classical LMS is reduced noise in the weight vector update. The value of the weight vector update on the  $q$ th iteration for the  $r$ th reference channel is expressed

$$\Delta w_{r(q)}(\tau) = \int_{(q-1)T_{int}}^{(q)T_{int}} e(t) \cdot N_r(t-\tau) dt \quad (2.2.3)$$

where  $\tau$  is the delay variable, and  $T_{int}$  is the integration time, during which the weight vector remains unchanged.

The weight vector update is summed with the weight vector from the previous iteration to form the new weight vector,  $w_{r^{(q)}}(\tau)$ , according to Equation 2.2.2. Every element in the weight vector corresponds to a unique delay at the delay line. Thus the product of each weight vector element with the appropriate delay produces a convolution. On the  $q$ th iteration, the sum over all  $R$  reference noise channels of these convolution results produces the estimate,  $y^{(q)}(t)$ , to the noise term in the main channel, where

$$y^{(q)}(t) = \sum_{r=0}^R \int_{T_{proc}}^{T+T_{proc}} (w_{r^{(q)}}(\tau) \cdot N_r(t-\tau)) d\tau \quad (2.2.4)$$

Here,  $T$  is the temporal length of each delay line, and  $T_{proc}$  is the processing time for the computer to collect the integration data, add the weight vector update to the previously stored values, and to establish communication with the delay line. Now  $y^{(q)}(t)$  is subtracted from  $d(t)$  to form the error signal in Equation 2.2.3 and the next iteration begins. Iterations continue until the algorithm has converged to a solution.

### 3.0 MADOP Design Considerations

**3.1 Overall Considerations.** The long term goals outlined in Table I were based on the requirements of an operational system while the short term goals were deemed sufficient to demonstrate the concept of optically based adaptive jamming cancellation. Thus, we designed the MADOP to provide two processing channels which demonstrate 30 dB cancellation of a 10 MHz bandwidth noise source at the C-band system IF of 80 MHz. The short term goal of achieving a loop lock time of 500 msec is sufficient to demonstrate the processing speed of the system. The personal computer is currently the main system bottleneck in processing speed. Dedicated electronics satisfying the long term speed goal of 5 msec would replace the personal computer in an operational system.

### 3.2 In-Line vs Mach-Zehnder Time Integrating Correlator.

Optical processors are well suited to performing the computations described in 2.2. For several years, optical time integrating correlators have been studied<sup>14-18</sup> for their potential application to such computational tasks as that presented in Equation 2.2.3. If the estimate from Equation 2.2.4 could be optically computed, then perhaps an all-optical implementation of the LMS algorithm would be possible. Two multichannel optical time integrating correlator architectures were considered for the MADOP system in order to compute  $\Delta w_r^{(q)}(\tau)$  from Equation 2.2.3. The competing subsystems were an in-line vs a Mach-Zehnder interferometric architecture.

**3.2.1 In-Line Time Integrating Correlator.** The in-line system shown in Figure 3.2.1.a has a single beam path. The input signal to the AO device generates a diffracted beam which is frequency shifted by the carrier frequency,  $f_c$ , of the signal. The diffracted beam is a plane wave imaged onto a linear CCD array. A reference beam at frequency  $f_{ref}$  generates a second plane wave imaged onto the CCD array and interacts with the signal beam.

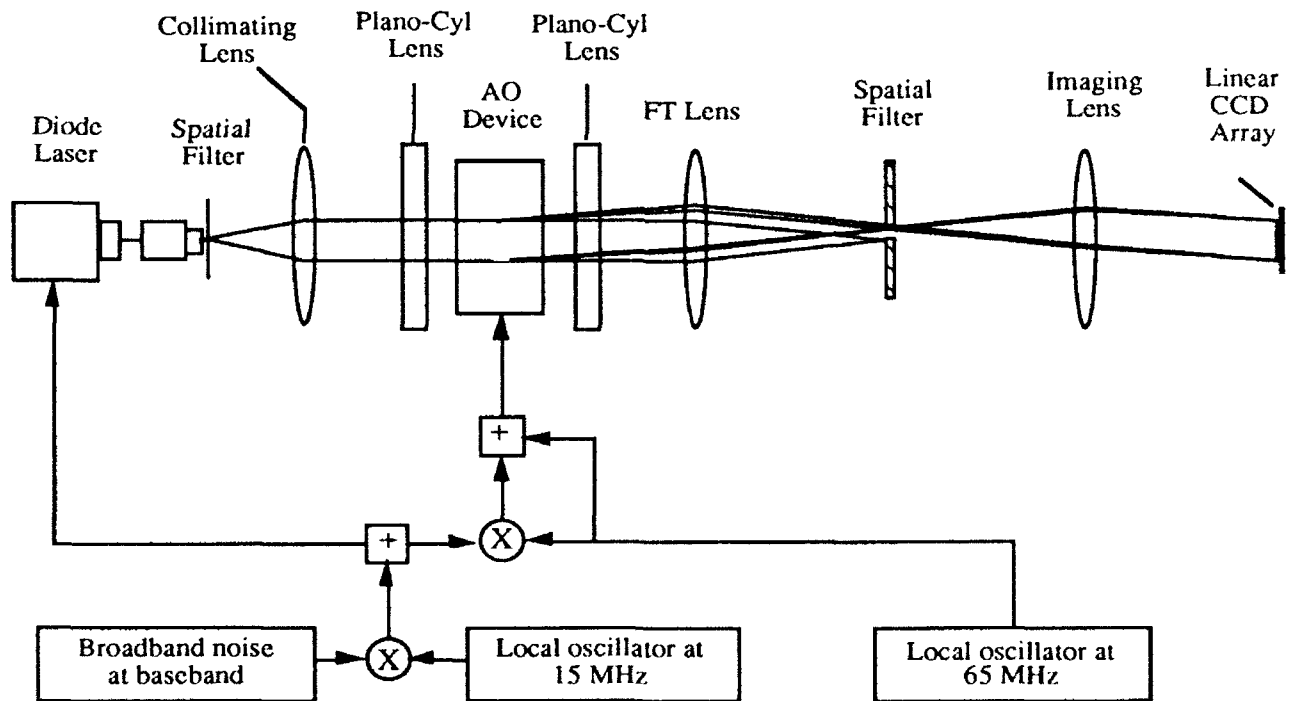


**Figure 3.2.1.a: In-Line Time Integrating Correlator.** The in-line architecture uses an electronically generated reference beam and the noise signal beam to perform a time integrating correlation.

These two plane waves recombine at an angle on the CCD array, producing



an intensity pattern which varies temporally and spatially,  $I(x,t)$ . Conceptually, this can be thought of as a periodic intensity function which sweeps by a fixed point at the difference frequency  $f_c - f_{ref}$ . VanderLugt fully develops this argument<sup>19</sup> and describes  $I(x,t)$  mathematically as

$$I(x,t) = B_1 + B_2 \cdot \cos[2\pi \cdot (f_c - f_{ref}) \cdot (t - T/2 - x/v_a)] \quad (3.2.1.1)$$

where  $B_1$  and  $B_2$  are intensity parameters dependent on the amplitudes of the two plane waves,  $t - T/2$  is the time parameter as measured from the center of the delay window, and  $v_a$  is the acoustic velocity of the AO cell.

The amplitude modulated laser strobes the moving intensity function. If the laser is being modulated at the difference frequency,  $f_c - f_{ref}$ , the grating appears stationary to an integrating detector such as the eye or a CCD camera. This process is the fundamental mechanism of optical time integrating correlation.

Typically the undiffracted beam is used as the reference, and thus  $f_{ref}=0$ . However, in our case it was not feasible to use the undiffracted beam as a reference. The AO cell had a time aperture of  $T=5 \mu\text{sec}$ , and the length of the 512 element CCD array was 13.3 mm. Since  $f_c - f_{ref}=80 \text{ MHz}$ , a correlation using the undiffracted beam as a reference would have generated a spatial carrier frequency at the CCD array of  $f_s=80 \text{ MHz} * 5 \mu\text{sec} / 13.3 \text{ mm}=30 \text{ mm}^{-1}$ . So the period of the spatial carrier is  $33 \mu\text{m}$ . However, the pixel size on the CCD array is  $26 \mu\text{m}$ . Hence attempts to image the entire  $5 \mu\text{sec}$  time aperture onto the CCD array prove unsuccessful because the spatial carrier is not sampled at the Nyquist minimum of at least two detector pixels per period.

To offset this problem we introduced an electronic reference into the AO cell driving signal as shown in Figure 3.2.1.a. The electronic reference generated a second diffracted beam with  $f_{ref} = 65 \text{ MHz}$ , thus yielding a spatial carrier period of 5.6 mm, which the CCD array adequately sampled. The frequency of the electronic reference is tunable, giving us control of the spatial carrier period.

Figure 3.2.1.a shows the optical and signal generation circuits used to perform an autocorrelation of a noise signal. Using this design, the RF input spectrum to the AO cell appears as shown in Figure 3.2.1.b. The local oscillator frequencies are selected so as to ensure that the lower sideband (shown at 55 MHz) falls outside the operating frequency range of the AO cell, ie. below  $f_{cutoff}$ .

The input spectrum to the diode laser is the same noise signal centered at 15 MHz from DC.

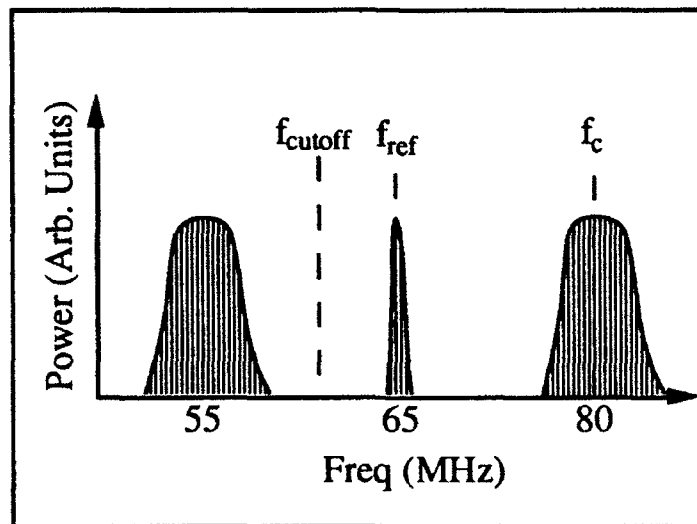


**Figure 3.2.1.b: RF Input Spectrum to AO Device for In-Line System.** The electronic reference,  $f_{ref}$ , is selected to be above  $f_{cutoff}$ , a characteristic of the bandpass for the AO device.

The in-line architecture has several inherent advantages over the Mach-Zehnder architecture, described in the following section. Unlike the interferometric design of the Mach-Zehnder correlator, the in-line system does not depend on interference between the reference and signal beam, making the configuration relatively insensitive to normal room vibrations. Additionally, the in-line design requires fewer optical components and requires only one multichannel AO cell, thus reducing system complexity and size.

However, we felt that the advantages of the in-line correlator were outweighed by the disadvantage of requiring that the antenna signals be input at baseband rather than at the system IF. The signal inputs to the correlator come from the auxiliary antennas and from the error signal,  $e(t)$ , which is generated in the acousto-optic tapped delay line. Since these signals are all at IF, we felt that rather than use additional RF equipment to convert these input signals to baseband, we should consider the Mach-Zehnder interferometric correlator architecture. This would allow signal inputs at IF. The in-line design should be reconsidered if a high resolution CCD array (eg., 1024 pixels at 13  $\mu\text{m}/\text{pixel}$ ) could be obtained.

**3.2.2 Mach-Zehnder Time Integrating Correlator.** The Mach-Zehnder time integrating correlator, shown in Figure 3.2.2.a, relies on

interference between the signal beam and the reference beam to form a correlation intensity pattern. A CW laser is split into two optical paths, with an AO cell in each path. One cell is driven by the error signal, and the second cell is driven by an auxiliary antenna output.

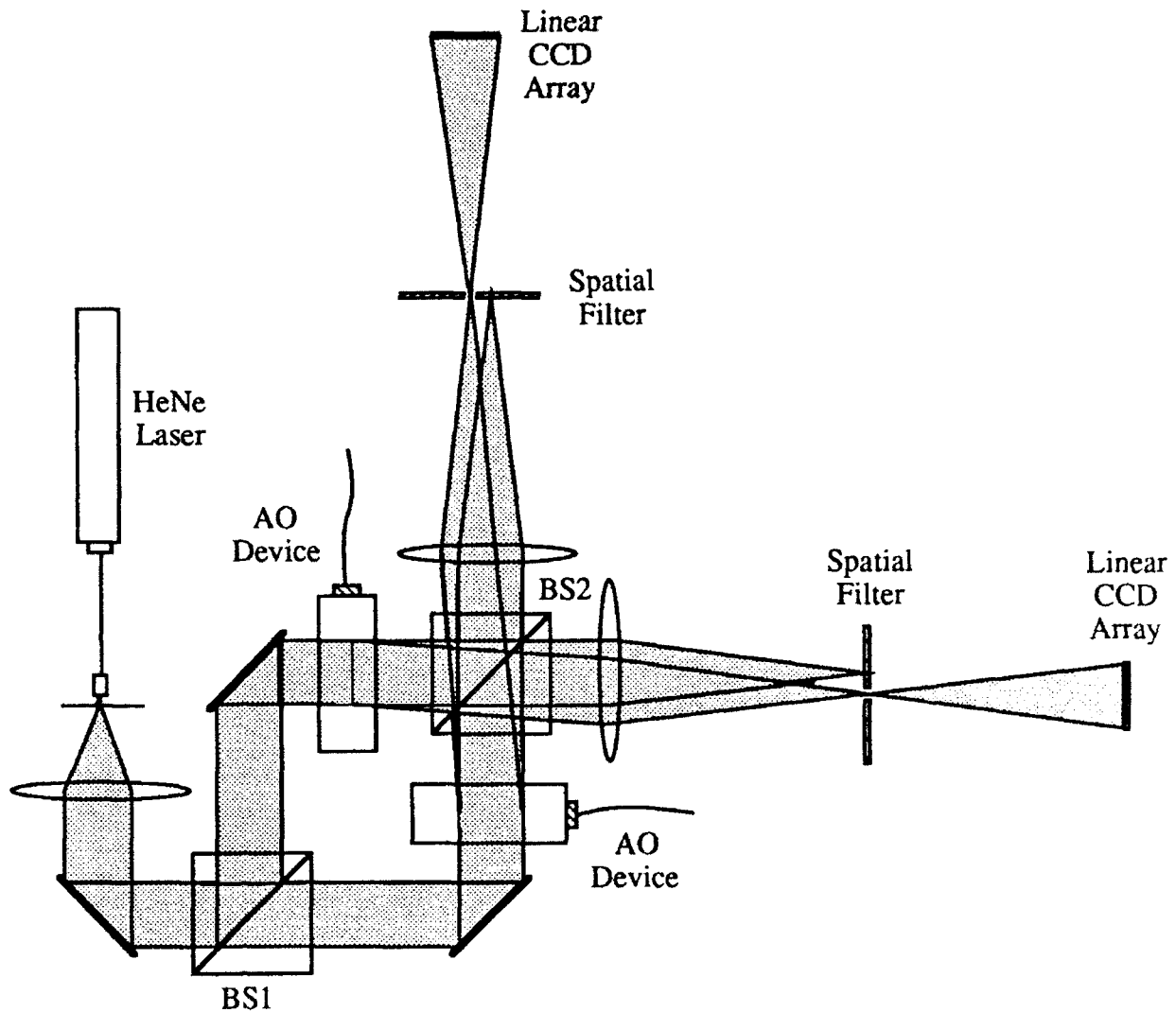


**FIGURE 3.2.2.a: Mach-Zehnder Interferometric Time Integrating Correlator.** The correlator uses an interferometer to set up a stationary spatial intensity pattern. Counter propagating AO cells perform the correlation.

The Mach-Zehnder interferometric time integrating correlator performs the computation of the correlation from Equation 2.2.3 in a straightforward manner. Referring to Figure 3.2.2.b, we see an RF carrier modulated by a square pulse as the input to an AO cell. The pulse acts as a diffraction grating propagating through the cell with velocity  $+v_a$ . Only the light which interacts

with this moving grating is diffracted into the +1 order. As the pulse moves, so does the portion of light which is diffracted. This causes a spot to scan across the CCD array with velocity  $-v_a$ . Now the same RF signal is introduced into a second AO cell in a counterpropogating direction, i.e., with velocity  $-v_a$ . Through the same process just described, this produces a second scanning spot which moves across the CCD array with velocity  $+v_a$ .

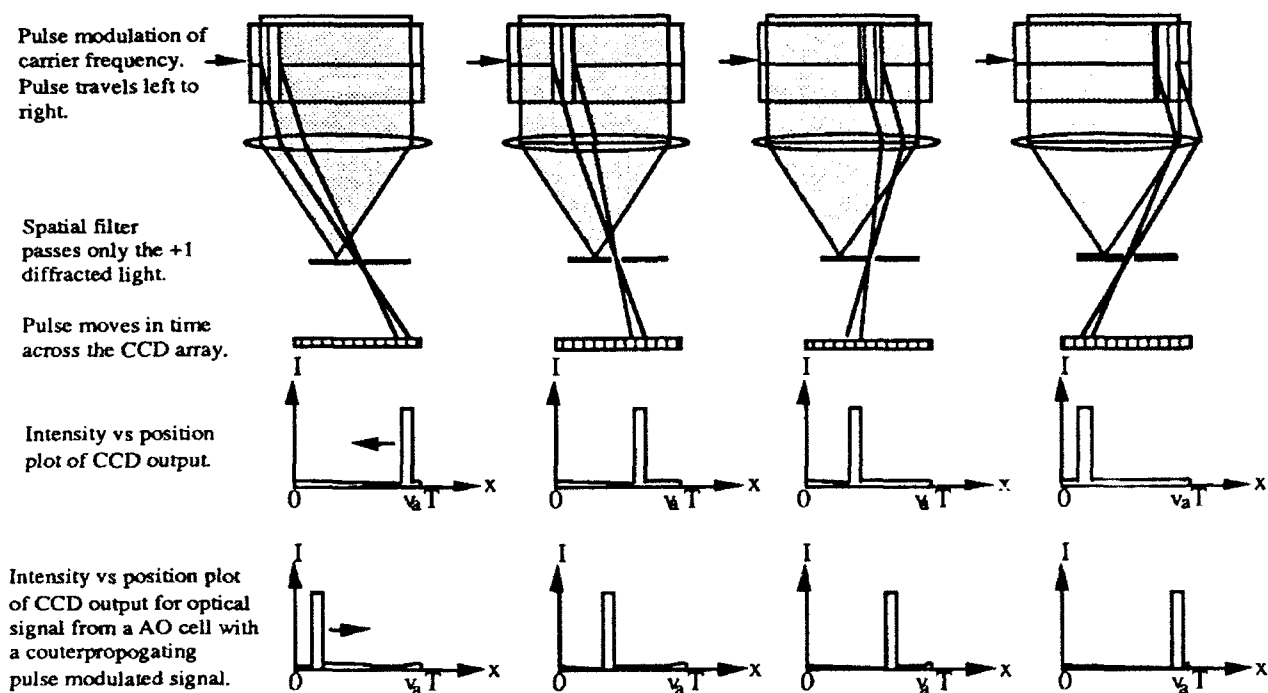


**Figure 3.2.2.b: Conceptual Diagram of Autocorrelation with Mach-Zehnder Interferometric Time Integrating Correlator.** The AO cells in the correlator are oriented so that the acoustic pulses counterpropagate. These counterpropogating pulses create counterpropogating optical beams which sweep by one another and build up the intensity pattern on the CCD array. The time integrated CCD output represents the correlation between the two RF input signals.

These two scanning spots move in opposite directions on the CCD array with equal speed. The CCD array integrates for a time  $T_{int}$ , during which the scanning spots pass over one another many times. The light intensity builds up on the CCD array in the region of overlap. Since the scanning spots are at the same optical frequency, they produce interference fringes. The fringe spacing, which serves as a spatial carrier here, may be adjusted through rotation of the beamsplitter BS2<sup>11</sup>. We hope that this conceptual explanation of the operation of the Mach-Zehnder interferometric time integrating correlator will complement the more rigorous treatment provided in other references<sup>14-19</sup>, including our own paper which presents the correlator design in more detail<sup>20</sup>.

The main advantage this architecture has over the in-line correlator is its ability to process RF signals at the system IF. Another unique benefit of using the interferometric correlator is that the effective correlation window is doubled due to the fact that the scanning spots are counterpropagating. Hence, two AO cells with a time aperture of 5  $\mu$ sec would produce a correlation window of 10  $\mu$ sec<sup>11</sup>. Finally, as with the in-line correlator, the Mach-Zehnder correlator has a tunable spatial carrier.

As we found during fabrication of the MADOP, the major drawback of the Mach-Zehnder correlator is vibration sensitivity. Since the spatial carrier is generated interferometrically, we found that even voice generated air currents were sufficient to disturb the correlation. The finished correlator is now being operated within a sealed table enclosure on a pneumatic vibration isolation table. All openings into the enclosure were sealed up because the correlator demonstrated sensitivity to air currents coming through any openings on the enclosure panels. A second disadvantage relative to the in-line correlator is that the Mach-Zehnder has a substantially more complex architecture, requiring two AO cells rather than one. In a multichannel application with multichannel AO cells costing more than \$15,000, this is an important consideration. In hindsight, the in-line correlator may have proved a better design choice for the correlator architecture.

**3.3 Acousto-Optic Tapped Delay Line Alternatives.** The AO tapped delay line consists of a programmable spatial light modulator (SLM), an AO delay line, a photodetector, and the associated optical components. As described in Section 3.2, the correlation between the main channel and each of the auxiliary channels is computed by the time integrating correlator. This produces an updated weight vector,  $w_i^{(q)}(\tau)$ , for each auxiliary channel. According to Equation 2.2.4, the sum of the products of these weight vectors with their corresponding auxiliary signals yields the estimate,  $y^{(q)}(t)$ , to the composite noise contained in the main channel.

The multiplication operation takes place by using an SLM to modulate a CW input beam to form taps on the AO delay line. These taps must be placed at precise delay locations and each tap must have a proper amplitude weighting. The sum of the product of each tap with its corresponding delay is accomplished by using a lens to collect all the light from the delay line onto a photodetector.

During Phase I of the MADOP in-house effort, we examined various off-the-shelf SLMs for use in forming the optical taps.<sup>1-7</sup> None of the tested devices

provided the required speed, contrast ratio, dynamic range, or overall system light efficiency. Thus we turned to the concept of using an AO deflector as an SLM. We have also examined using a programmable laser diode array to form the weight vector.<sup>23</sup>

**3.3.1 Use of Acousto-Optic Spatial Light Modulator (AOSLM).** The concept of using an acousto-optic deflector as a spatial light modulator originated in 1983 with Frederick Freyer.<sup>21</sup> An AO deflector will generate an output beam propagating at a unique angle for each frequency component of the RF input spectrum. As shown in Figure 3.3.1.a, a simple lens system ensures that all output beams are parallel with one another. An RF input spectrum (consisting of a set of amplitude weighted frequency components) produces a set of parallel-propagating amplitude weighted optical beams. These beams form the taps on the AO delay line.

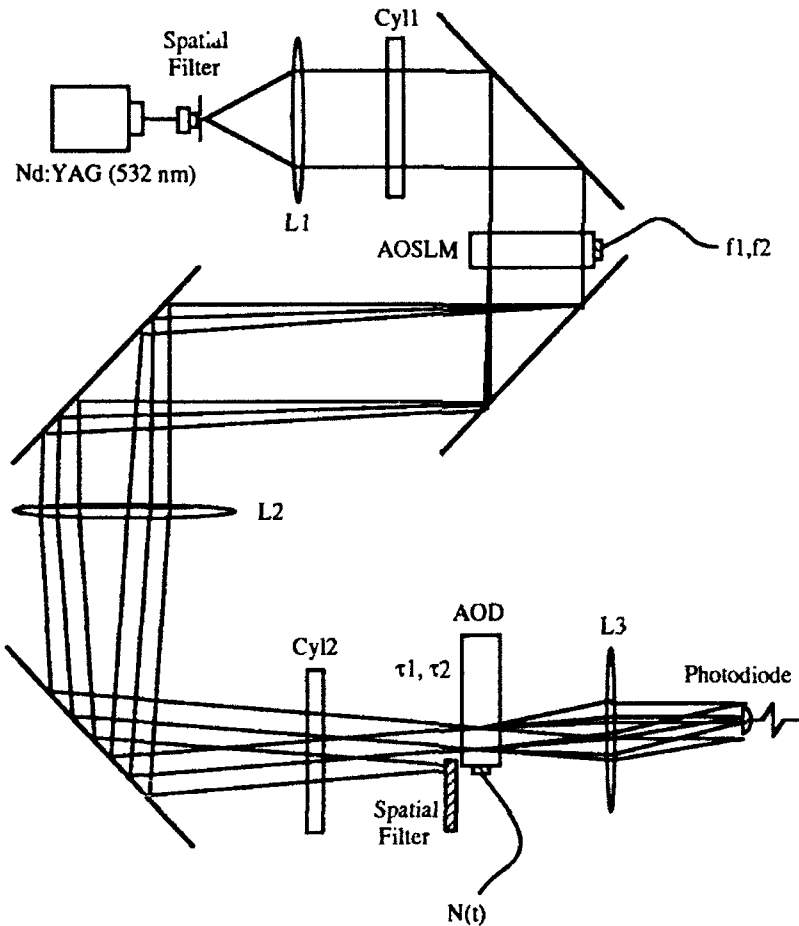


**Figure 3.3.1.a Acousto-Optic Spatial Light Modulator Used to Tap Acousto-Optic Delay Line.** RF frequency inputs  $f_1$  and  $f_2$  generate two diffracted beams which tap the delay line at two corresponding delays,  $\tau_1$  and  $\tau_2$ .

**3.3.1.1 Selection of Optical Components for Delay Line.** The AO devices used for the AOSLM and the delay line were Brimrose TeO<sub>2</sub> longitudinal mode eight channel deflectors with a bandwidth BW=40 MHz, centered at f<sub>c</sub>=80 MHz. We needed to design an optical system which scanned 5 μsec of delay on the delay line using the full range of deflection angles generated by the AOSLM. Referring to Figure 3.3.1.1.a we observe that a frequency sweep across the bandwidth, BW, of the AOSLM, from f<sub>c</sub>-0.5\*BW to f<sub>c</sub>+0.5\*BW produces a range of deflection angles θ<sub>min</sub> to θ<sub>max</sub> according to the relationships

$$\begin{aligned}\theta_{\min} &= (\lambda/v_{\text{AOSLM}}) * (f_c - 0.5*BW) \\ \theta_{\max} &= (\lambda/v_{\text{AOSLM}}) * (f_c + 0.5*BW)\end{aligned}\quad (3.3.1.1.1)$$

where v<sub>AOSLM</sub> is the acoustic velocity and λ is the optical wavelength.

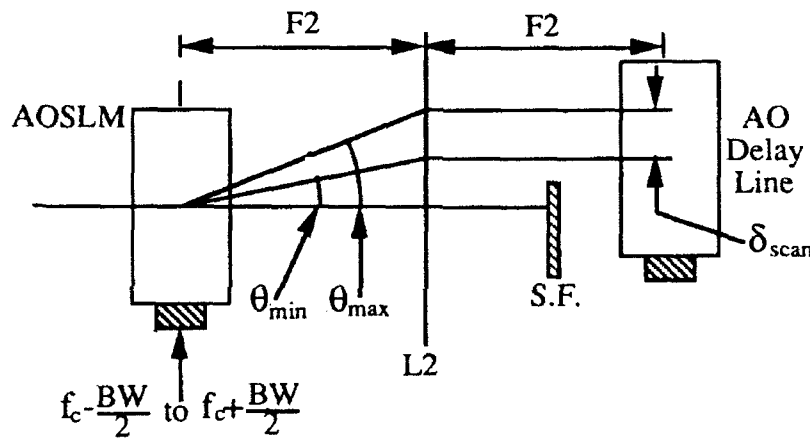


**Figure 3.3.1.1.a** Bandwidth of AOSLM Sets Angular Deflection Range,  $\theta_{\max} - \theta_{\min}$ , and the Scan Range,  $\delta_{\text{scan}}$ . The frequency scanning bandwidth of the AOSLM device creates an angular scan which in turn generates a spatial scan on the AO delay line.

Approximating the distance from lens L2 to the center of the AOSLM as the focal length F2, we find that the scan distance,  $\delta_{\text{scan}}$ , on the AO delay line is

$$\delta_{\text{scan}} = F2 * (\text{TAN}(\theta_{\max}) - \text{TAN}(\theta_{\min})) \quad (3.3.1.1.2)$$

Now since  $\theta_{\max}$  and  $\theta_{\min}$  are  $< 20$  mrad, we make a small angle approximation and substitute into Equation 3.3.1.1.2 from Equation 3.3.1.1.1 to obtain

$$F2 \approx \delta_{\text{scan}} * v_{\text{AOSLM}} / (\lambda * BW) \quad (3.3.1.1.3)$$

We can also express  $\delta_{scan}$  as the product of the total delay range,  $\tau$ , and the acoustic velocity of the delay line,  $v_{delay}$ , such that

$$F2 = (\tau * v_{delay} * v_{AOSLM}) / (\lambda * BW) \quad (3.3.1.1.4)$$

Thus, if we want to map an AOSLM frequency scan range of 60-100 MHz onto a delay range of 5  $\mu$ sec using a 532 nm laser and  $v_{AOSLM} = v_{delay} = 4.2$  mm/ $\mu$ sec, then  $F2 = 4145$  mm. Clearly, this is not practical. If we constrain  $F2 \leq 750$  mm due to size limitations on the overall system, then the delay range will be limited to  $\tau \leq 0.935$   $\mu$ sec. If  $\tau = 0.935$   $\mu$ sec then  $\delta_{scan} = 3.9$  mm, and if the input beam diameter,  $D2$ , into the AOSLM is 20 mm then the diameter,  $A2$ , of this lens must be  $A2 \geq D2 + \delta_{scan} = 23.9$  mm.

According to our design requirements in Table I, we need  $\tau = 5$   $\mu$ sec. In order to accomplish this with lenses of reasonable focal length, we must alter other variables in equation (11). In particular, we consider using a slow shear mode AO deflector with  $v_{AOSLM} = 0.617$  mm/ $\mu$ sec and  $BW = 40$  MHz as the AOSLM device. This device could provide the required delay range of 4.93  $\mu$ sec using a lens L2 with  $F2 = 609$  mm, and  $A2 \geq 40.7$  mm. Such a device has been ordered for a Phase III upgrade to the existing system.

Our next concern is selecting lens L3 which collects the diffracted and undiffracted light for heterodyne detection on the photodiode. Figure 3.3.1.1.b shows two AOSLM generated taps addressing the AO delay line.

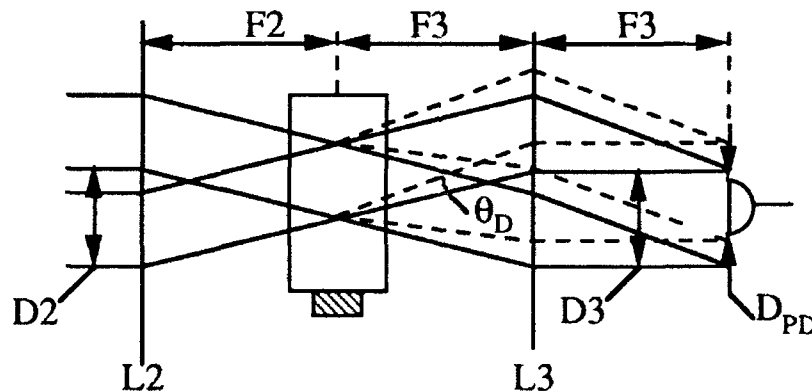


**Figure 3.3.1.1.b Two Optical Taps Addressing AO Delay Line.** The two optical taps generated by the AOSLM, both of diameter  $D2$ , are focused into the AO delay line by lens L2. Lens L3 collimates both the diffracted and undiffracted beams from both taps. A photodiode is placed at the region where the diffracted and undiffracted beams overlap.



Two beams of diameter  $D_2$  are focused by lens  $L_2$  into the AO delay line. Lens  $L_3$  collects the undiffracted beams, collimates them, and causes them to overlap completely with diameter  $D_3$  at one focal length,  $F_3$ , from  $L_3$ . Similarly, all the +1 order diffracted beams propagating at a maximum deflection angle of  $\theta_D$  overlap completely with one another at a distance  $F_3$  from  $L_3$ . A photodiode with diameter  $D_{PD}$  is placed in the region where the diffracted and undiffracted beams overlap, as shown in Figure 3.3.1.1.b. The set of overlapping diffracted beams are displaced from the set of overlapping undiffracted beams by an offset  $\Delta$ , as shown in Figure 3.3.1.1.c, where

$$\Delta = F_3 * \text{TAN}(\theta_D) \approx F_3 * \theta_D \quad (3.3.1.1.5)$$

Additionally, we see that the length of the overlap region (crosshatched area in the figure) between the diffracted and undiffracted beams is  $D_3 - \Delta$ .

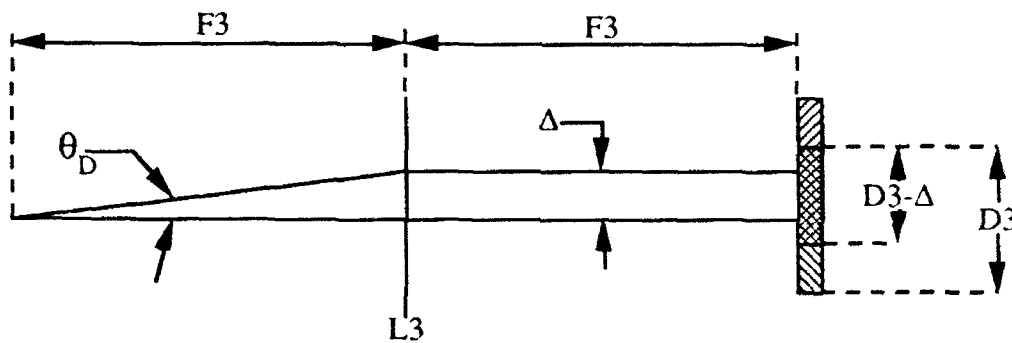


**Figure 3.3.1.1.c Size of Overlap Between Undiffracted and Diffracted Beams at the Photodiode.** The rays separated by distance  $\Delta$  represent the central rays of the diffracted and undiffracted beams passing through the AO delay line. Both beams have a diameter of  $D_3$ . They overlap in the focal plane of lens  $L_3$ .

Therefore, we demand that for all deflection angles  $\leq \theta_D$  that the length of the overlap region be no greater than the photodiode diameter, that is

$$D_3 - \Delta \leq D_{PD} \quad (3.3.1.1.6)$$

We know that

$$(D_2 / D_3) = (F_2 / F_3) \quad (3.3.1.1.7)$$

and that we can express the maximum deflection angle  $\theta_D$  as

$$\theta_D = \lambda * f_{MAX} / v_{delay} \quad (3.3.1.1.8)$$

where  $f_{MAX}$  is the upper end of the signal bandwidth for the delay line input. Thus, from Equations 3.3.1.1.5 to 3.3.1.1.8, we can compute a maximum value for F3

$$F3 \leq D_{PD} / ((D2 / F2) - (\lambda * f_{MAX} / v_{delay})) \quad (3.3.1.1.9)$$

In the case of a longitudinal mode AOSLM discussed earlier which limits  $\tau < 1 \mu\text{sec}$ , we have  $D2 = 20 \text{ mm}$ ,  $F2 = 750 \text{ mm}$ ,  $\lambda = 532 \text{ nm}$ , and  $v_{delay} = 4.2 \text{ mm}/\mu\text{sec}$ . For our application,  $f_{MAX}=85 \text{ MHz}$ , and the ThorLabs DET-2 photodiode has a diameter of  $D_{PD} = 1 \text{ mm}$ . Hence,  $F3 \leq 63 \text{ mm}$ . If F3 exceeds 63 mm, then the displacement  $\Delta$  becomes too large relative to the beamsize D3 and the overlap between the undiffracted and diffracted beams becomes smaller than the photodiode diameter.

The diameter, A3, of the lens L3 must be large enough to collect light from the entire scan range,  $\delta_{scan}$ , plus it must account for the beam width D3 and the displacement  $\Delta$ . Therefore

$$A3 \geq \delta_{scan} + D3 + \Delta \quad (3.3.1.1.10)$$

For the case just described,  $A3 \geq 6.3 \text{ mm}$ . Now if a shear mode AOSLM is used, then  $\tau \leq 4.9 \mu\text{sec}$ ,  $F2 = 600 \text{ mm}$ , and lens L3 has  $F3 \leq 44.3 \text{ mm}$  and  $A3 \geq 22.7 \text{ mm}$ .

**3.3.1.2 AOSLM Signal Generation Requirements.** To generate a single tap, a programmable RF frequency synthesizer (e.g., the HP 8360) produces a single frequency output at a specified amplitude. This signal is amplified and used as the RF input to a channel of the AOSLM. Ideally, if the line scan camera at the output of the time integrating correlator is an array of  $1 \times N$  detector elements, we would like to reproduce N uniquely weighted taps on the delay line. Thus, the AOSLM requires N unique programmable frequency sources. This could be accomplished by means of N frequency stable voltage controlled oscillators (VCOs) driven by an N channel programmable power supply. With  $N=512$ , this equipment intensive signal generation requirement represents a major drawback in using an AOSLM for this application.

An option which reduces this signal generation requirement is to maintain the "book-keeping" of the N element weight vector in the computer, but only use

a few of the largest components to form taps on the delay line. Stephen Welstead conducted studies into the potential impact of limiting the number of tap positions that are simultaneously tapped with the AOSLM.<sup>10</sup> For the purpose of his research, he assumed that a maximum of eight simultaneous taps would be used. He developed and modeled a sequential algorithm which operated within these limits and yet demonstrated adequate cancellation. This approach also had convergence speeds that were orders of magnitude faster than a "pure" steepest descent approach in which all elements of the weight vector were used in every iteration. This result is not entirely surprising when one considers that for a signal composed of four delayed versions of the noise, the optimal weight vector will have only four non-zero components.

Using this "limited resolution" output weight vector approach significantly reduces the signal generation requirement for the AOSLM driving signals. Figure 3.3.1.2.b depicts the signal generation scheme for the case of N=4.

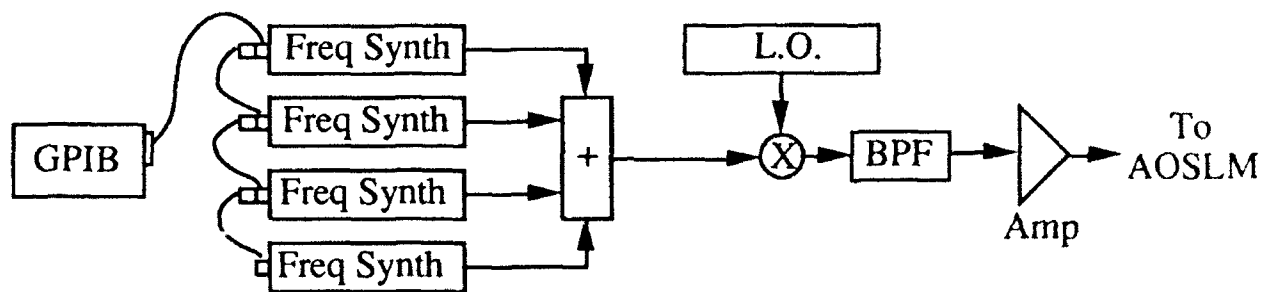


**Figure 3.3.1.2.b Signal Generation Scheme for AOSLM Driving Signals With Four Output Weights.** These four programmable frequency synthesizers are mixed up to the center frequency of the AOSLM. Each synthesizer generates a single amplitude weighted tap at the AO delay line.

What are the requirements for the frequency synthesizers? Assume the AOSLM has a frequency stepping bandwidth of BW, and that the AO delay line has an acoustic velocity of  $v_{\text{delay}}=4.2 \text{ mm}/\mu\text{sec}$ , with a center frequency of  $f_c=80 \text{ MHz}$ , and a maximum delay of  $\tau=5 \mu\text{sec}$ . Also assume that the AOSLM must point the tap on the 80 MHz RF carrier with a resolution of  $10^\circ$  or better with a stability of  $\pm 2^\circ$ . Thus, the spatial resolution of taps,  $x_{\text{res}}$ , required at the delay line is given by

$$x_{\text{res}} = (10^\circ/360^\circ) * (v_{\text{delay}}/f_c) = 1.46\text{E-}3 \text{ mm}$$

Thus, the resolution of the frequency steps of the frequency synthesizer must be

$$f_{\text{res}} \leq \text{BW} * x_{\text{res}} / (v_{\text{delay}} * \tau) = \text{BW} * 6.95\text{E-}5 \text{ MHz}$$

The frequency stability,  $\delta f$ , of the frequency synthesizer must be

$$\delta f = (2^\circ/10^\circ) * f_{res} = f_{res}/5 = BW * 1.39E-5 \text{ MHz}$$

For  $BW = 40 \text{ MHz}$ ,  $f_{res} = 2.78 \text{ kHz}$ , and  $\delta f = 0.556 \text{ KHz}$ ; and for  $BW = 10 \text{ MHz}$ ,  $f_{res} = 0.695 \text{ KHz}$ , and  $\delta f = .139 \text{ KHz}$ .

Based on earlier analysis<sup>7</sup>, we need weight elements with at least 100 (and preferably 1000) unique amplitude values. However, in the present implementation the A/D board after the correlator is only 8-bit. Therefore, the programmable frequency synthesizer should at least provide 256 unique amplitude steps in order to be comparable to the A/D resolution. For a maximum RF output power of  $P_{MAX}$ , the minimum stepsize for the output power is

$$P_{res} \leq P_{MAX}/256$$

So if  $P_{MAX} = 10 \text{ mW}$ , then  $P_{res} = 0.04 \text{ mW}$ .

Various GPIB controllable signal generators and frequency synthesizers manufactured by Hewlett Packard, Fluke, and Anritsu provide  $BW=40 \text{ MHz}$ ,  $f_{res}=3.0 \text{ KHz}$ ,  $\delta f=0.5 \text{ KHz}$ ,  $P_{MAX}=10 \text{ mW}$ , and  $P_{res}=0.1 \text{ mW}$ . This meets all requirements except for the minimum stepsize for output power, but the system should still work even with this larger stepsize. The Rome Lab Equipment Pool currently has four HP 3325A waveform synthesizers in stock. The 3325A is limited to frequencies less than 20 MHz, so the output would need to be mixed with a stable oscillator and bandpass filtered about 80 MHz prior to the AOSLM, as shown in Figure 3.3.1.2.b.

As discussed above, if the frequency synthesizer is limited to only 10 MHz bandwidth, then the frequency resolution and stability must increase to  $0.695 \pm 0.139 \text{ KHz}$  to achieve the required tap resolution over a  $5 \mu\text{sec}$  range on the delay line. These requirements can be relaxed to  $3.5 \pm 0.7 \text{ KHz}$  if the delay range is reduced to  $1 \mu\text{sec}$ . Thus, for a proof of concept demonstration using the HP 3325A, we recommend limiting the total delay range to  $1 \mu\text{sec}$  and operating the 3325A from 10-20 MHz and the local oscillator at 65 MHz, and using the 10 MHz Daden bandpass filter to reject the l.o. and the lower sideband.

We have published additional details of the AOSLM design previously.<sup>1,4,5,11,12,20</sup> Additionally, Mr. Robert Berinato has written a paper which rigorously describes the AOSLM operating theory.<sup>22</sup> The interested reader is

referred to these publications for further information on the AOSLM.

**3.3.2 Use of a Programmable Laser Diode Array.** We are considering using a programmable laser diode array as an SLM in this application. Light from the array would be focused into the delay line, with each laser element tapping a unique delay, as shown in Figure 3.3.2.a. This would form the weight vector. Unlike the AOSLM, this approach does not limit the MADOP to simultaneously using only eight components of the weight vector. For example, in a multichannel delay line application, an  $N \times 100$  element array could simultaneously tap up to 100 delays on each of  $N$  channels of a multichannel AO deflector. We elaborate on the summary presented here in Reference 23.

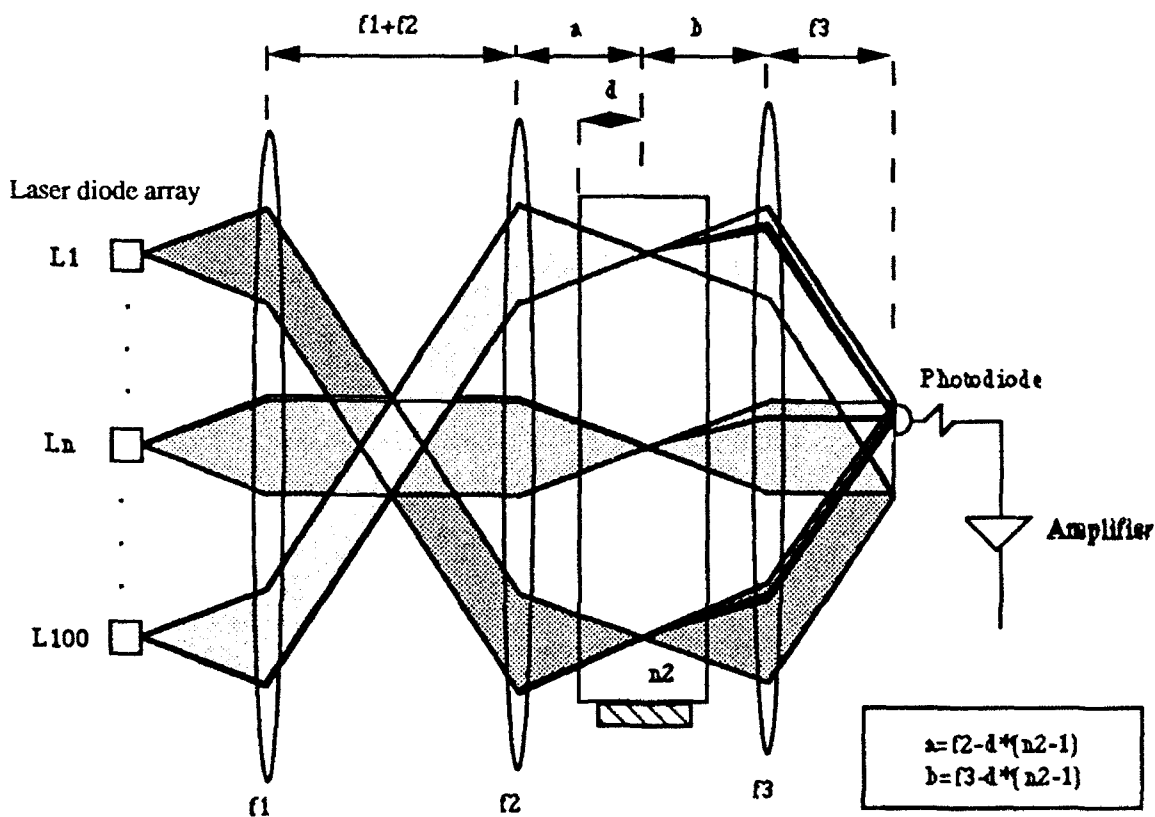


**Figure 3.3.2.a Programmable Laser Diode Array Forming Optical Taps onto AO Delay Line.** A laser diode array, nominally of 100 elements, forms sharply focused taps on an AO delay line. The black shaded beams represent the diffracted light copropagating with undiffracted light which are heterodyne detected at the photodiode.

We performed a proof-of-concept demonstration of this concept using two laser diode devices. The set-up for this experiment is shown in Figure 3.3.2.b.

The lens labelled  $f_1$  (in Figure 3.3.2.b) focuses the collimated beams into the center of the acoustic beam in the delay line. As described elsewhere<sup>24</sup>, the maximum diffraction efficiency occurs when the  $1/e^2$  beam spot diameter within the AO delay line satisfies the condition  $d=\Lambda_s/2$ .  $\Lambda_s$  is the acoustic wavelength at a given carrier frequency. Since

$$\Lambda_s = v_s/f_c \quad (3.3.2.1)$$

where the carrier frequency  $f_c = 80$  MHz and the acoustic velocity  $v_s=3.96$  mm/msec. This results in  $\Lambda_s=50 \mu\text{m}$ . Based on this, we expected a spot diameter of  $d=25 \mu\text{m}$  to produce maximum diffraction efficiency. From the relationship

$$d = 4\lambda f_1/\pi D \quad (3.3.2.2)$$

where  $\lambda$  is the laser wavelength and  $D$  is the  $1/e^2$  diameter of the collimated beam=6.3 mm, we need  $f_1=197$  mm. Experimental measurements of heterodyned signal strength as a function of the depth of focus (using focal lengths of: 100, 125, 150, 200, 250, 300 mm) verified that indeed, maximum diffraction efficiency is obtained for a lens with  $f_1=200$  mm.

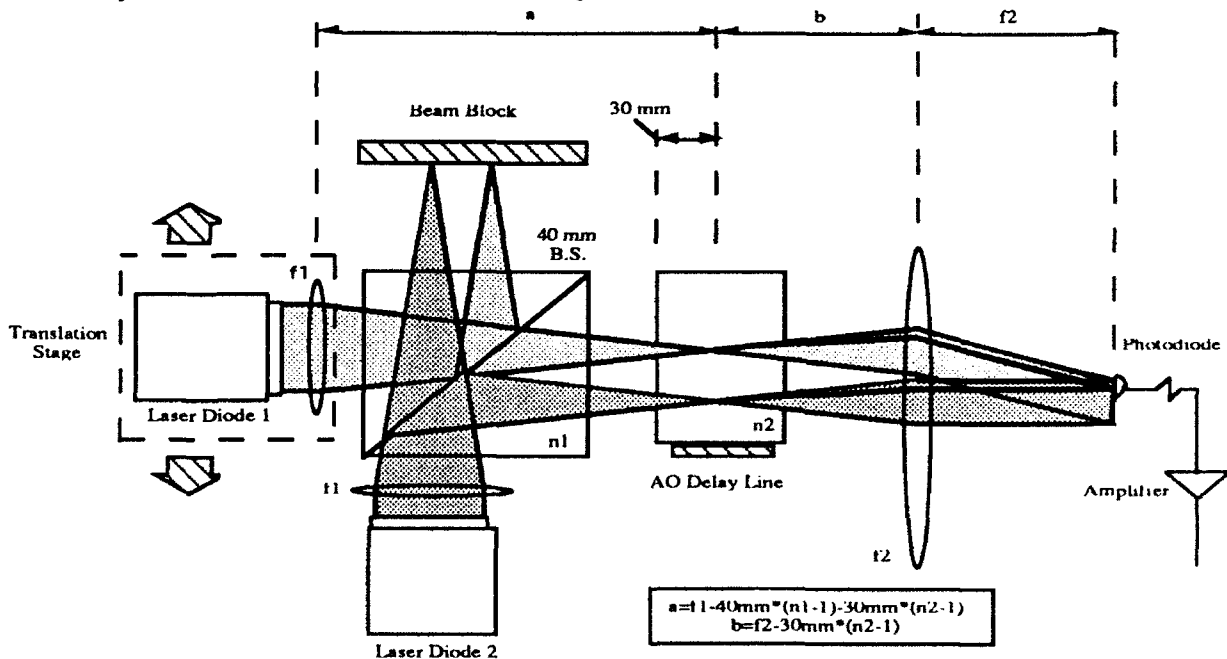


**Figure 3.3.2.b Proof-of-Concept Demonstration of Using a Programmable Tapped Delay Line Using a Laser Diode Array.** A laser diode on a translation stage is sharply focused into an AO delay line. Translating this laser moves the tap position and thus the corresponding delay of the RF signal. A second laser source taps a fixed delay in the delay line. The black shaded beams represent the diffracted light copropagating with the diffracted light.

Referring to Figure 3.3.2.c, with our large input spot size and fast lens the focusing angle  $\phi$  is large enough to ensure that the Bragg condition is satisfied for a cone of angles,  $\delta\theta_B$  within the focused beam. In fact, depending on  $\phi$  and the incidence angle of the incoming beam, there may actually be two regions of diffraction at  $\pm\theta_B$ , as shown in the figure. A photodetector at position C collects undiffracted light originating from position B and upshifted diffracted light originating from position A. These two beams are parallel propagating waves which are heterodyne detected, thus recovering the difference frequency. A similar phenomenon occurs when the photodetector is placed at position D where the frequency downshifted light is collected.

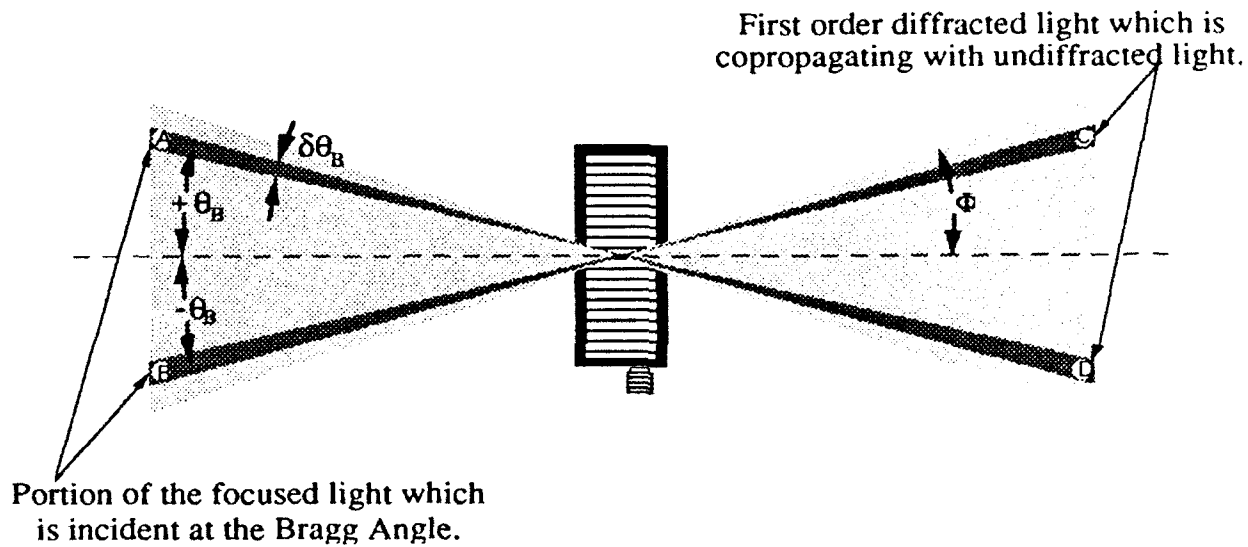


**Figure 3.3.2.c: Geometry of Sharply Focused Optical Tap.** The focusing lens has an angle of focus  $\phi$ . If  $\phi$  is large enough, and depending on the orientation of the AO delay line, there may be two regions of diffraction, where  $\theta_B$  is the Bragg angle.

Now as the optical tap is moved to another delay the detected signal moves off of the photodetector which is located at position C. In order to collect the frequency upshifted light from all tap positions, a second lens,  $f_2$ , is positioned as shown in Figure 3.3.2.b. Since the upshifted light (and its copropagating undiffracted light) is diffracted at a constant angle for all tap positions, this lens directs this light into a single spot, where the photodetector is located. In order for heterodyne detection to occur, the two interacting waves must overlap and be almost parallel to one another. The geometry of the system just described satisfies this requirement because a portion of the reference beam (unshifted,

undiffracted light) is collinear to the signal beam (up/downshifted, diffracted light) for all tap positions.

To demonstrate the ability of the translating laser to tap delays across the time aperture of the AO delay line, we use an HP Model 83623A Synthesized Sweeper to generate a 1  $\mu\text{sec}$  pulse with 5  $\mu\text{sec}$  repetition on an 80 MHz carrier. The output from the synthesizer is split prior to amplification. One copy of the signal serves as a reference input to the Tektronix 11403 Digitizing Oscilloscope, the other copy is amplified and drives the AO delay line. The laser tap is positioned such that the amplified photodiode output which is input into the oscilloscope registers zero delay relative to the reference. The tap is moved to address delays of 1.0, 2.5, and 4.0  $\mu\text{sec}$ . The resultant oscilloscope traces are shown below in Figure 3.3.2.d. If we expand the time scale and observe the 80 MHz carrier, we verify that both the carrier and the pulse modulation experience true time delay as a function of tap position.

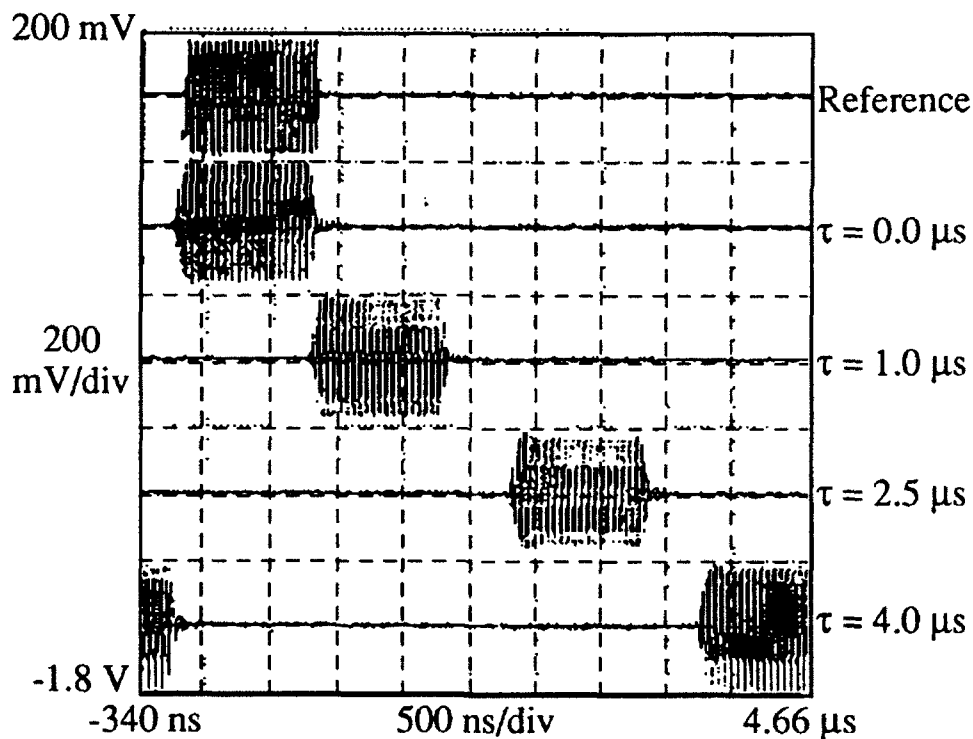


**Figure 3.3.2.d Oscilloscope Trace of Time Delay Generated for Four Unique Tap Positions.** Laser in proof of concept architecture is translated and forms taps of a pulsed RF signal at delays ranging from 1-4  $\mu\text{sec}$  relative to a reference channel.

Furthermore, the amplitude of the delayed pulse remains quite uniform over the



entire delay region. To quantify this observation, we measured the power of the heterodyned output from the photodiode as a function of tap position. This data is presented in Figure 3.3.2.e. The flat amplitude response is largely a function of the fine positioning of lens f2 and the photodiode relative to the AO delay line.

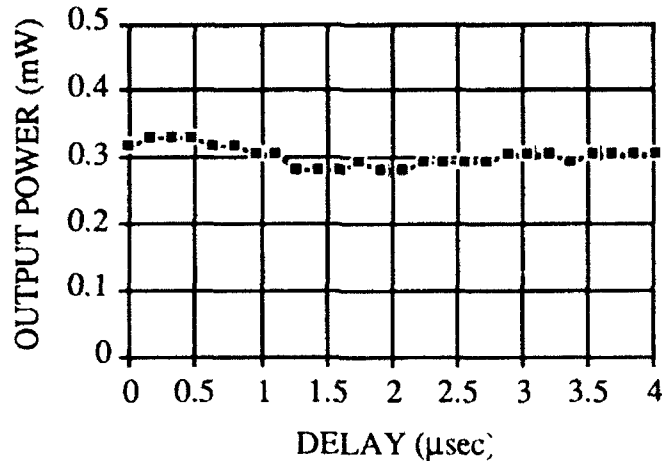


**Figure 3.3.2.e Amplitude Response of Heterodyne Detected Pulses as a Function of Tap Position.** The different tap positions over a 4 μsec delay range on the AO delay line have a flat amplitude response.

VanderLugt<sup>25</sup> describes the photodetector current resulting from the heterodyne detection of two overlapping plane waves on a photodetector as

$$g(t) = A_s D_{PD} S + A_r D_{PD} S + (2SA_s A_r) \cdot \text{sinc}(\pi \theta_D D_{PD} / \lambda) \cdot \cos(2\pi f_c t) \quad (3.3.2.3)$$

where  $S$  is the detector responsivity,  $D_{PD}$  is the diameter of the photodetector,  $\theta_D$  is the angle between the signal and reference beam, and  $A_s$  and  $A_r$  are the amplitudes of the signal and reference beams, respectively. The standard AO-based heterodyne detection system uses a system of beamsplitters and mirrors to split off a reference beam prior to the AO device and recombines it with the signal beam just prior to detection. As the RF power,  $P$ , is increased, the amplitude of the diffracted signal beam changes but the amplitude of the undiffracted signal remains unchanged. However, in the case of the heterodyne detection system shown in Figures 3.3.2.a and 3.3.2.b in which the reference and signal beams copropagate through the AO device,  $A_r$  is also coupled to the RF power, thus leading to nonlinear behavior.

For example, at a fixed RF power level, let the amplitude of the diffracted signal beam be  $A_s = m \cdot A_0$ , where the  $m$  is the modulation index as a function of RF power and  $A_0$  is the incident optical amplitude of the beam within the cone of angles  $\delta\theta_B$ , originating from position A in Figure 3.3.2.c, which experiences

Bragg diffraction. The relationship between the modulation index, diffraction efficiency,  $\eta$ , and RF power is expressed as

$$m = \eta^{1/2} = \sin((\alpha P)^{1/2}) \quad (3.3.2.4)$$

where  $\alpha$  is a physical constant relating to the geometry and material properties of the AO device. At position C, this diffracted beam interacts with undiffracted reference light within a cone of angles  $\delta\theta_B$  (originating from position B) with amplitude  $A_r = (1-m) \cdot A_0$ . Thus, at position C, for  $(\alpha \cdot P)^{1/2} < \pi/2$ , when the RF power increases the amplitude of the diffracted beam increases in proportion to  $m$  and the amplitude of the undiffracted beam decreases as  $1-m$ .

The impact of this expected nonlinearity will be studied in the Phase III MADOP effort. The negative aspects of this nonlinear behavior will be weighed against the positive benefit of reduced system size, weight, and complexity relative to the classical architecture which uses beamsplitters and mirrors to generate the reference beam. A second shortcoming of this approach is that the laser diode array cannot address a continuum of delays because the lasing elements are uniformly spaced at discrete positions.

**3.4 Interface Techniques.** The ideal implementation for the MADOP would be an all analog optical system which avoids the time consuming analog to digital (A/D) conversions necessary in digital adaptive algorithms. Since the early 1980s, Rome Laboratory has sponsored several contracts with General Electric (GE) and Harris Corp. to examine all-optical implementations.<sup>26-32</sup> Additionally, during FY92, the Surveillance and Photonics Directorate had an effort to build an all-optical system in-house under JON 4600P105.<sup>33-36</sup> If the key advantage of an all-optical system is speed, the key disadvantage is the weakness of optical integrator technology.

**3.4.1 All-Optical Interface.** The shortcomings of optical integrators limit the usefulness of an all-optical interface within the MADOP. These limitations result in extremely limited system bandwidth, an overall reduction in system reliability, and limited extension to multichannel operation.

The GE system from the early 1980s used a Hughes Liquid Crystal Light Valve (LCLV) to integrate the correlation result. The LCLV has a "write" and a "read" side. For sinusoidal input signals, this correlation pattern forms a periodic grating on the "write" side. The incident light collects on the "write" side and changes the reflectivity of the "read" side. Thus, the "read" side now has a diffraction grating representative of the correlation result. An optical beam

diffracts from the grating on the "read" side and forms optical taps on the delay line.<sup>37</sup>

The current GE effort, the Harris effort, and the above mentioned in-house program, all use photorefractive crystals (PRCs), such as BaTiO<sub>3</sub>, BSO, and InP as the optical integrator. The net effect of the PRC integrator is identical to that of the LCLV. The correlation result forms a diffraction grating in the crystal material and a read beam diffracts from the grating, forming optical taps on the delay line. See Reference 33 for details of the PRC integrator.

Both optical integrators, LCLVs and PRCs, depend on the formation of a high efficiency diffraction grating within the integrator material. Such gratings are readily obtained from the autocorrelation of a monotone sinusoidal RF input signal. The autocorrelation of a sinusoidal input signal forms a continuous sinusoidal grating, which produces high efficiency diffraction upon illumination. Hence, these optical integrators should work well in the adaptive cancellation of sinusoidal signals from a single source.

However, as the bandwidth of the input signal broadens, the physical size of the correlation becomes localized, dropping the total amount of light diffracted. For example, the spatial size of the autocorrelation of a 50 KHz bandwidth noise source is 50 times narrower than the autocorrelation of a 1 KHz bandwidth source. Section 4.1.2.1 explains this concept in more detail. The important result is this: optical integrators have yet to demonstrate a reproducible test which demonstrates acceptable performance for other than narrowband signals. Dr. Robert Montgomery, the primary investigator on the Harris effort, emphasizes that the strength of his system is speed and compact size, but readily admits that his system will only work for narrowband noise sources.<sup>38</sup>

On a more subjective note, we have found the LCLV to be rather unreliable. We obtained two devices from GE as contract residue from the AOAP effort. One device did not work at all. The second device was unable to resolve even the largest pattern on an Air Force resolution chart. Furthermore, the LCLV requires a specialized driver which generates an asymmetric square wave. The details of the LCLV testing are contained in Reference 33.

**3.4.2 Computer Controlled Interface.** The rationale behind a computer controlled adaptive processor is to use the parallel computation power of optics in tandem with the bookkeeping power of the computer. The computationally intensive wide-bandwidth correlation from Equation 2.2.3 is computed optically and collected in a linear CCD array. The CCD output (the

weight vector update) is digitized and processed on a personal computer. Calibration factors are added to correct for amplitude non-uniformities. The results are then added to the weight vector stored in the computer memory. The computer uses the updated weight vector to control the spatial light modulator (SLM), thus forming the optical taps on the delay line. A thorough description of the system hardware and software is deferred until Section 4.3.

Flexibility and ease of use make the computer controlled interface an excellent choice for the proof-of-concept MADOP design. Off the shelf components are readily obtained to control the CCD cameras, perform the A/D conversion, and interface with test equipment via GPIB. Furthermore, we are able to write custom software to perform simple post processing tasks such as noise reduction on the collected CCD data. However, these benefits come at the expense of speed. While the computer controlled interface is useful in the initial design and testing phases of the MADOP program, a different solution is necessary to reach the long term loop lock speed. As described in the next section, we feel that dedicated electronics which replace the computer functions would provide a several order of magnitude improvement in operating speed.

**3.4.3 Custom Electronic Interface.** A third option for the interface between the optical time integrating correlator and the AO tapped delay line is a custom electronics package. This method is a refinement of the computer controlled interface in which the computer is replaced with dedicated electronic components.

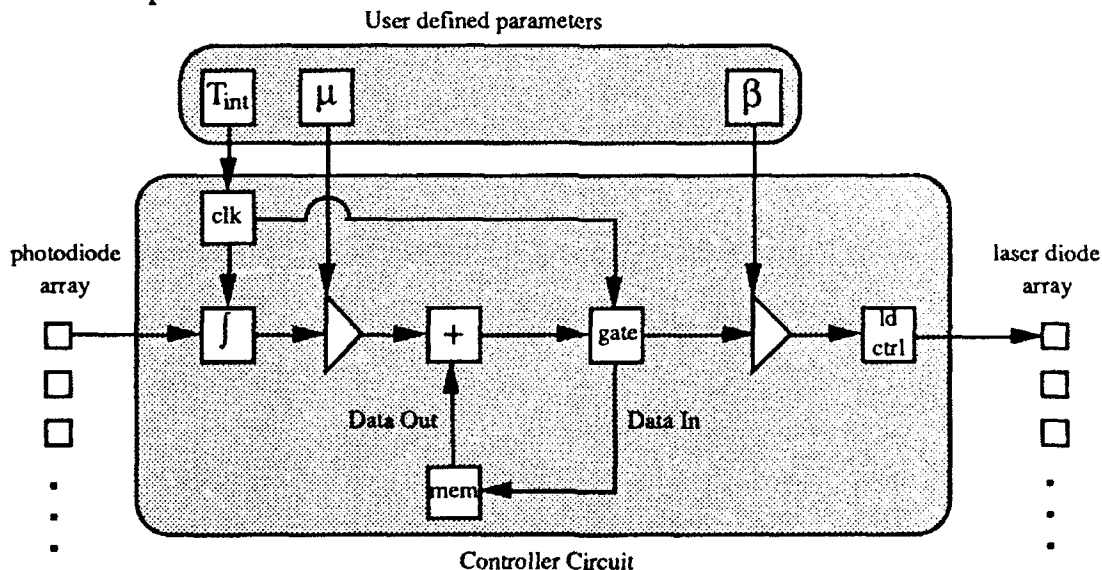


**Figure 3.4.3.a Analog Circuit to Control Laser Diode Array with Photodiode Array Output.** The user defines the integration time,  $T_{int}$ , step-size,  $\mu$ , and calibration factor,  $\beta$ .

Referring to the circuit in Figure 3.4.3.a, a linear array of photodiodes collects light from the correlator. Each photodiode in the array integrates for a time interval,  $T_{int}$ , and forms a single element in the weight update vector,  $\Delta w_{i(q)}(\tau)$ . As described by Equation 2.2.2, this element is multiplied by a step-size parameter,  $\mu$ , and electronically summed with the previously computed weight vector,  $w_{i(q-1)}(\tau)$ , stored in a memory buffer. Each pixel has a user-set calibration factor,  $\beta$ , to compensate for spatial light non-uniformities in the MADOP system. This calibration factor controls the amplification of the signal driving the corresponding laser diode in the laser diode array.

This analog circuit avoids the time-costly A/D operations of the computer controlled interface. The user can set the integration time, the step size, and the calibration factor. A description of an experiment demonstrating the concept of using a programmable laser diode array as an SLM appears in Section 3.3.2.

### 3.5 Use of Neural Network Algorithm for Tap Selection.

This investigation considered the feasibility of using neural networks to perform some of the signal processing required for closed loop operation. The original intent was to feed a trained neural network the correlation and have it determine the  $n$  best tap locations. It was thought that since neural networks showed promise for the monotone case (where cancellation involved learning a spatial phase shift of the correlation) that this approach may be extended to more complex correlation results <sup>8,9</sup>.

Preliminary investigation of the wide band case concluded that a neural network approach was not practical. The essentially infinite variety of correlation results which can be imaged upon the photodiode array necessitates an exceptionally large training sets for a standard backpropagation neural network. Other neural network implementations were considered (primarily, a probabilistic neural network) but these, too, fell short due to the impracticality of developing a training set to recognize arbitrary correlation results. As such, the decision was made to forego a neural network approach in favor of utilizing specific tools to perform less general signal analysis. A description of these tools and the results obtained through their use, appear in Section 4.3.

## 4.0 Fabrication and Testing of MADOP Subsystems.

### 4.1 Multichannel Time Integrating Correlator.

**4.1.1 Hardware Description.** Based on the considerations presented in Section 3.2, we chose a Mach-Zehnder interferometric time integrating correlator architecture as shown in Figure 3.2.2.a. Referring to this figure, a Melles Griot 05-LHP-991 10 mW CW HeNe laser serves as a source. A Newport model 910 spatial filter followed by a 200mm focal length achromat and an iris aperture stop produce a collimated beam 20 mm in diameter. A 1" AR coated non-polarizing beamsplitting cube (BS<sub>1</sub>) splits the incident light into two beam paths.

One path contains a multichannel AO deflector (AO<sub>1</sub>) where two channels are driven by replicas of the main channel signal, and the other path contains a multichannel AO deflector (AO<sub>2</sub>) where each of two channels is driven by a separate auxiliary channel signal. These AO devices are Brimrose Corporation eight channel TeO<sub>2</sub> longitudinal-mode deflectors. They have a 5.0  $\mu$ sec time aperture and a 30 MHz bandwidth centered at 95 MHz which is wide enough to encompass our 10 MHz noise signals centered at 80 MHz. The AO devices are mounted on z-rotation mounts to adjust for Bragg diffraction conditions. As discussed in Section 3.2.2, these cells are also oriented so as to have counterpropagating acoustic beams. The full beam illuminates the acoustic aperture of both AO devices. We select the two channels which have the maximum illumination by the input beam. One focal length away from each cell (adjusted for the optical path variance in the beamsplitter cube and the TeO<sub>2</sub> material of the AO devices) is a 200 mm focal length biconvex AR coated imaging lens.

A second 1" AR-coated non-polarizing beamsplitter cube (BS<sub>2</sub>) recombines the +1 order of the diffracted light from the two paths, and steers them through a spatial filter (at the Fourier plane of the imaging lens) and onto the linear CCD arrays. Since the two channels in the AO devices are at different heights, the heights of each CCD array are adjusted accordingly. According to Section 3.2.2, we want only the +1 diffracted order from each AO device to pass through a spatial filter in the focal plane of the imaging lens. Thus, the correlations are formed as the two counterpropagating scanning spots pass over the time integrating CCD array. Since the acoustic aperture is approximately 22 mm and the length of the 512 element CCD array is 13.3 mm, the CCD array should be placed 321 mm from the imaging lens in order to put all 5  $\mu$ sec of correlation information onto the detector. A short focal length plano-cylindrical lens can

focus the light in the vertical direction onto the detecting elements, thus boosting the signal to noise ratio. This entire architecture is mounted on a 2' x 3' optical breadboard.

**4.1.2 Test Results.** We performed several tests to demonstrate the performance of the correlator. We tested the ability of the system to compute the autocorrelation of wideband RF signals, the ability to resolve time delays between two correlated signals, and a demonstration of multichannel correlation<sup>20</sup>.

**4.1.2.1 Autocorrelation of Wideband Signals.** Pulsed test signals were generated by mixing the pulsed output from a LeCroy Model 9100 Arbitrary Function Generator (AFG) with an 80 MHz oscillator and amplifying to the proper signal level. The signal input was split and introduced into a single channel in both multichannel AO devices. Figure 4.1.2.1.a shows a 100 nsec pulse, 5  $\mu$ sec pulse repetition period, on the 80 MHz carrier, while Figure 4.1.2.1.b displays the RF spectrum of the same signal.

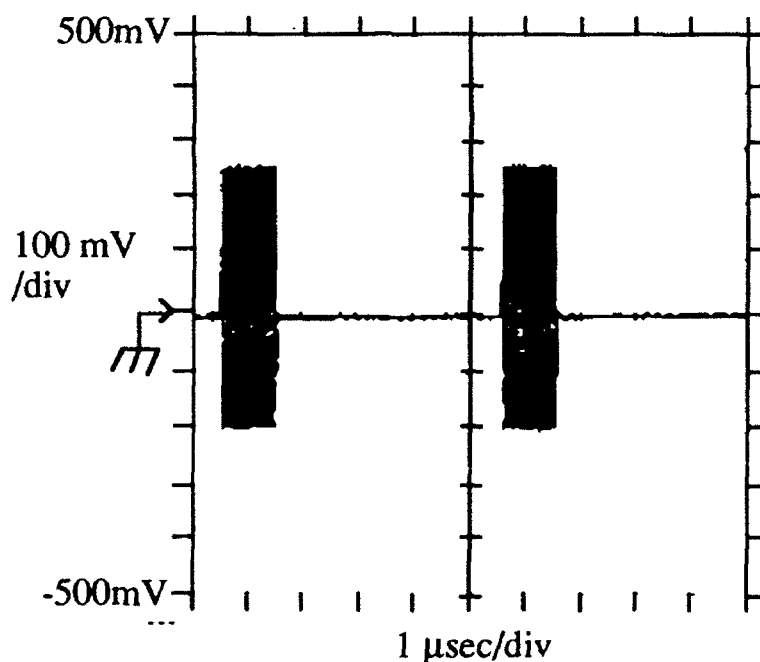


**Figure 4.1.2.1.a** Oscilloscope Trace of Pulsed Input, 1  $\mu$ sec Pulsewidth, 1  $\mu$ sec Pulsewidth, on 80 MHz Carrier. RF input to correlator to demonstrate wideband correlation performance.

The autocorrelation of this RF input is computed according to the description given in Section 3.2.2. The entire 5  $\mu$ sec time aperture of the AO

devices is imaged onto the line scan camera. The Girard 3197 board performs an 8-bit A/D conversion of this data, and our software package saves the data to disk in ASCII format. (Section 4.3 details the camera/computer interface and the software package.) The amplitude non-uniformities (measured using uncorrelated data) were subtracted, and the results for varying pulsewidths are



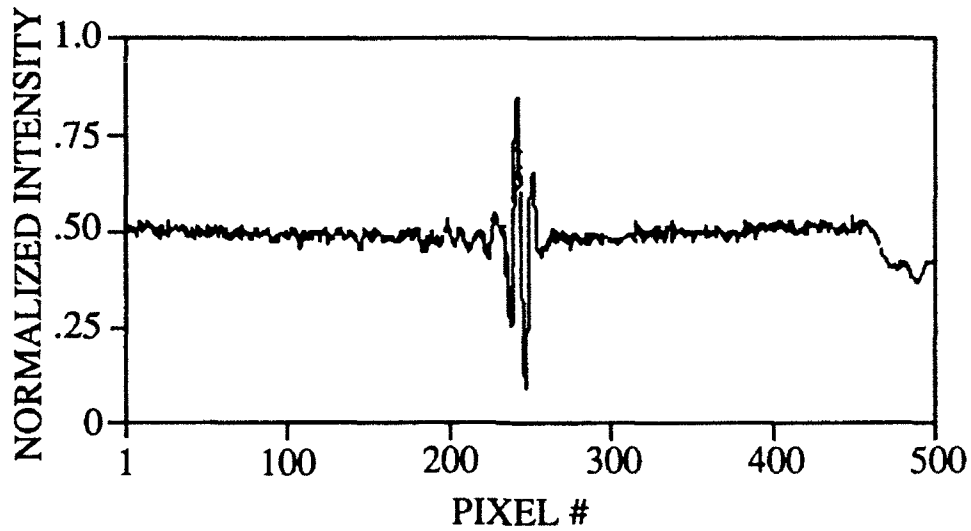


**Figure 4.1.2.1.c** Optically Computed Autocorrelation of 100 nsec Pulse on 80 MHz Carrier.

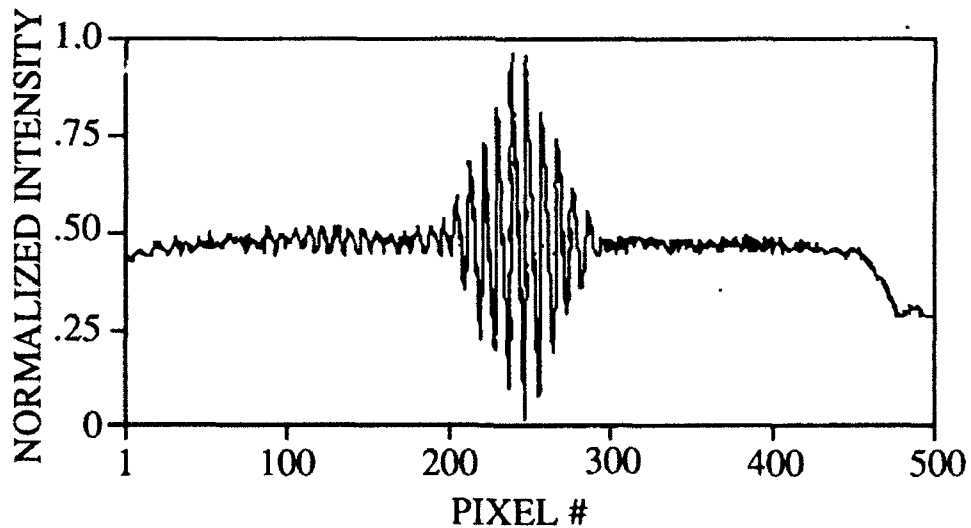


**Figure 4.1.2.1.d** Optically Computed Autocorrelation of 500 nsec Pulse on 80 MHz Carrier.

A second type of wideband signal was generated using a NoiseCom Model NC1107 A 100 MHz white noise source passed through a Daden Model DC80-10-3BMBM bandpass filter (10 MHz bandpass centered at 80 MHz.) The RF input spectrum is shown in Figure 4.1.2.1.f. We expect that a wideband noise signal of

bandwidth BW should have an autocorrelation equal to  $1/BW$  in the time domain. The optically computed autocorrelation of this test signal, shown in Figure 4.1.2.1.g, indeed shows a result corresponding to approximately 0.1  $\mu$ sec in width.

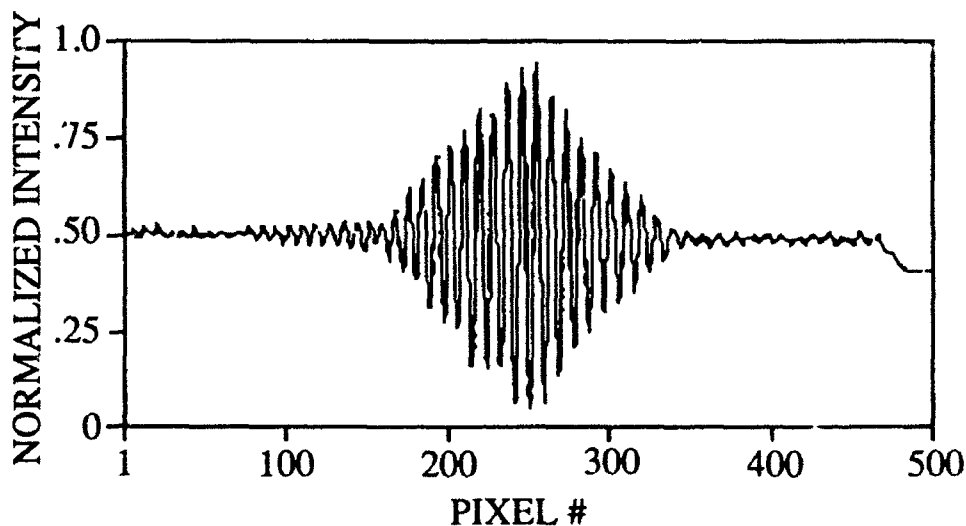


**Figure 4.1.2.1.e** Optically Computed Autocorrelation of 1000 nsec Pulse on 80 MHz Carrier.

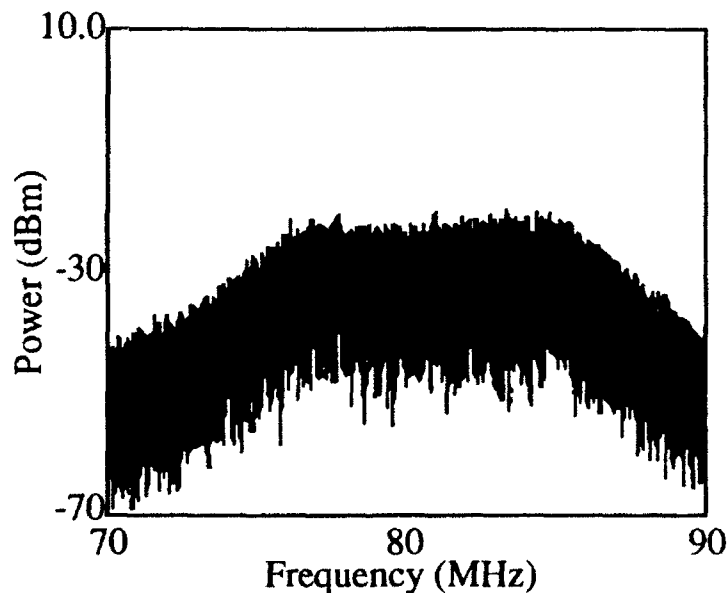


**Figure 4.1.2.1.f** RF Spectrum of Broadband Noise Signal. Noise spectrum used as input to correlator to demonstrate wideband correlation performance.

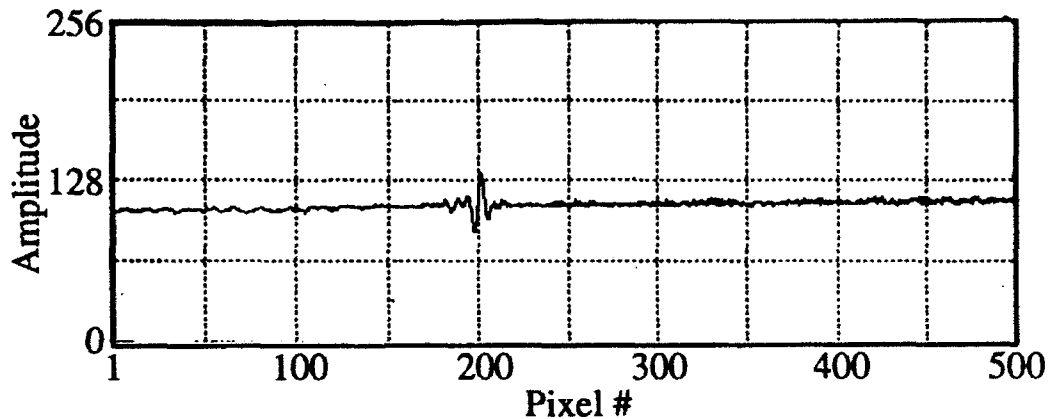


Figure 4.1.2.1.g Optically Computed Autocorrelation of a 10 MHz Noise Source.

**4.1.2.2 Autocorrelation With Delay and Multichannel Operation.** We purchased a set of Anderson Bulk Acoustic Wave (BAW) delay lines, Part Number 083020-506, which permitted us to put a delay in one of the RF inputs relative to the other input. Figure 4.1.2.2.a shows the signal generation scheme used. The main channel has a delay of  $\tau_1$ . The delay to one auxiliary channel has a relative delay of  $|\tau_2 - \tau_1|$  and the other auxiliary channel has a relative delay of  $|\tau_3 - \tau_1|$ . This test demonstrates the ability of the correlator to discriminate delays in each of the two channels, simultaneously.

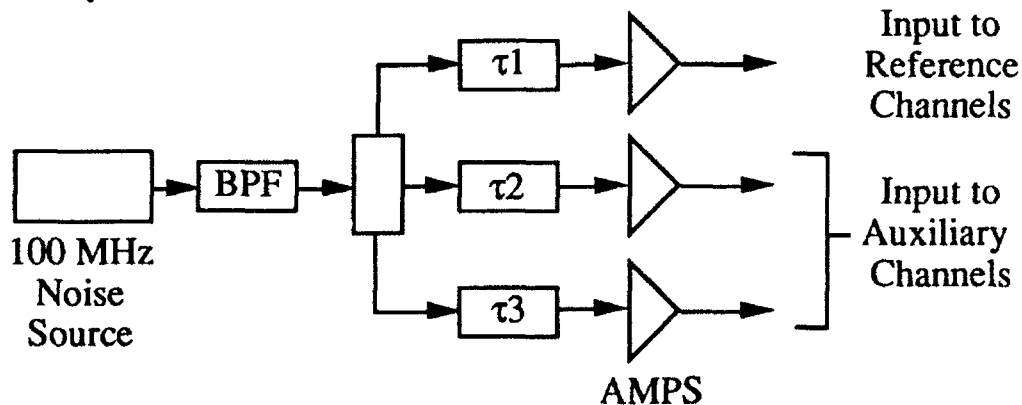
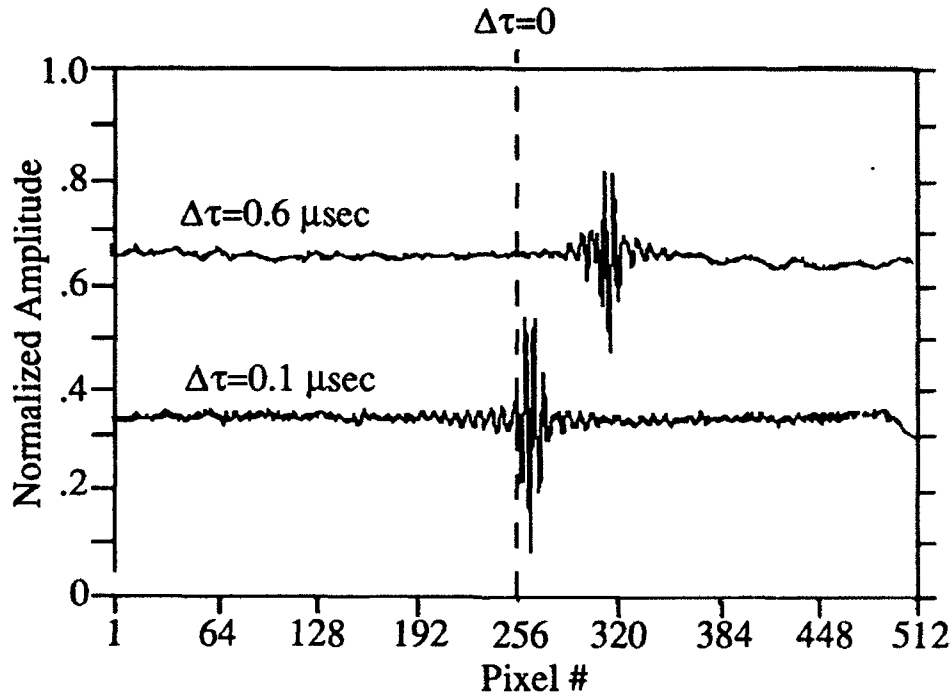


Figure 4.1.2.2.a Signal Generation Scheme for Multichannel Autocorrelation of Delayed 10 MHz Noise Signals.

The system was aligned such that zero delay corresponded to pixel #256 in the line scan camera. Thus, pixel 512 corresponds to a delay of +2.5  $\mu$ sec and pixel 1 corresponds to a delay of -2.5  $\mu$ sec. We used the 10 MHz noise source to collect the data shown in Figure 4.1.2.2.b. The upper correlation result had a

delay of  $\tau_2 - \tau_1 = 0.6 \mu\text{sec}$ . This displaced the correlation peak by about 73 pixels, which corresponds to a delay of  $.71 \mu\text{sec}$ .



**Figure 4.1.2.2.b Multichannel Autocorrelation of Delayed 10 MHz Noise Signal.** This data was collected simultaneously from two processing channels of the optical time integrating correlator. One auxiliary channel has a delay of  $0.6 \mu\text{sec}$  and the other auxiliary channel has a delay of  $0.1 \mu\text{sec}$  relative to the reference channels. (The bias offset is artificial for display purposes.)

The lower correlation result had a delay of  $\tau_3 - \tau_1 = 0.1 \mu\text{sec}$ , which displaced the peak by 11 pixels, or  $0.11 \mu\text{sec}$ . The uncertainty in this measurement is large, owing mostly to the arbitrary nature of selecting where the peak of the correlation occurs. Additional measurements are discussed and recorded in Reference 20.

## 4.2 Multichannel Tapped Delay Line.

**4.2.1 Hardware Description.** Section 3.3 describes the various alternatives considered for the AO tapped delay line. Section 3.3.1 describes the AOSLM tapped delay line architecture which was fabricated for the MADOP system.

Referring to Figure 3.3.1.a, an ADLAS model 200 diode-pumped, frequency doubled (532 nm) Nd:YAG 20 mW source is spatially filtered and collimated with an achromat, generating a 40 mm diameter collimated beam.

This beam illuminates the active channels of the AOSLM. The AOSLM device is an 8 channel Brimrose Model MTED-8 acousto-optic deflector with an 80 MHz center frequency, 30 MHz bandwidth, 22 mm spatial aperture, and 5  $\mu$ sec time aperture.

Lens L2, located a focal length from the center of the AOSLM, focuses all diffracted beams into the multichannel AO delay line. The beams are all parallel to one another and at the Bragg angle relative to the AO delay line. The AO delay line is a device identical to the AOSLM. A spatial filter blocks undiffracted light from the AOSLM allowing only diffracted light to form taps on the delay line. Lens L3 collimates the diffracted and undiffracted beams from the AO delay line and directs these parallel propagating beams onto a ThorLabs Model DET2 silicon photodiode. The detector is located in the region where the overlap of the diffracted and undiffracted beams is largest.

Plano-cylindrical lens Cyl1 focuses the light in the vertical direction into the AOSLM. The light is re-collimated in the vertical direction by lens L2. Lens Cyl2 focuses the light vertically into the delay line and lens L3 recollimates the light prior to the photodiode. See Section 3.3.1 and References 20 and 22 for additional details concerning the hardware.

**4.2.2 Test Results.** The AO tapped delay line has been thoroughly characterized.<sup>11,12,20,22</sup> Several key results are presented here.

We were concerned about the performance of the delay line architecture over the full range of tap positions. Since the optical taps are generated by driving the AOSLM with amplitude weighted monotone signals, we thought to test the delay line frequency response over the AOSLM bandwidth of 60-100 MHz. A Hewlett-Packard Model 83623A Synthesized Signal Generator was used to generate this monotone driving signal for the AOSLM. A Hewlett-Packard Model 8753C Network Analyzer with a Model 85046A S-parameter Test Set was used to generate the frequency sweep input to the delay line. The resulting data is displayed in Figure 4.2.2.a.

There is a 6 dB amplitude variation in the signal magnitude at a fixed AO delay line input frequency as the tap position is moved from  $\tau=0$  ( $f=60$  MHz) to  $\tau=1.0$   $\mu$ sec ( $f=100$  MHz). We believe this is due to a misalignment in the lens L3 relative to the photodiode and the AO delay line. Even the slightest misalignment (especially when the photodiode is not one focal length from L1) will result in position dependent amplitude non-uniformities because the diffracted and undiffracted beams will not have the same overlap on the photodiode. This effect

could be reduced by using a larger photodiode, which comes at the expense of reduced speed and increased noise.

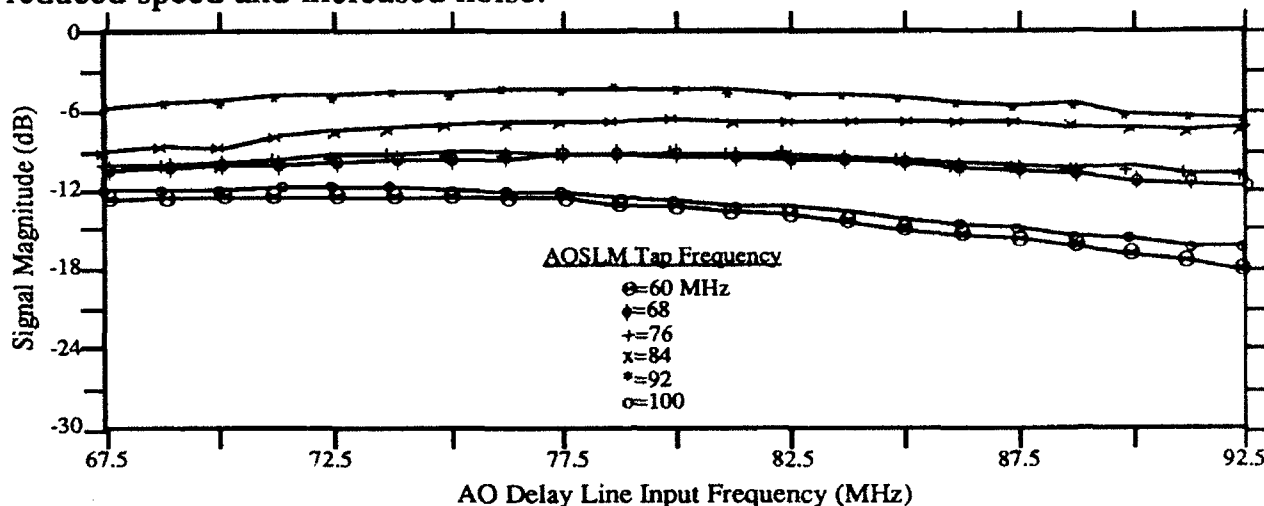


**Figure 4.2.2.a** Frequency Response of AO Tapped Delay Line as a Function of Tap Position. Tap position on AO delay line was varied by changing the frequency input to the AOSLM over the AOSLM bandwidth 60-100 MHz.

Additionally, we observe a non-linear frequency response over the delay line bandwidth of 67.5-92.5 MHz at a fixed tap position. This is seen more clearly in Figure 4.2.2.b in which the AOSLM tap frequency is fixed at 76 MHz. However, the MADOP is designed to operate at a 10 MHz bandwidth centered at 80 MHz. Over this range, the signal magnitude varies by less than +/- 0.1 dB.

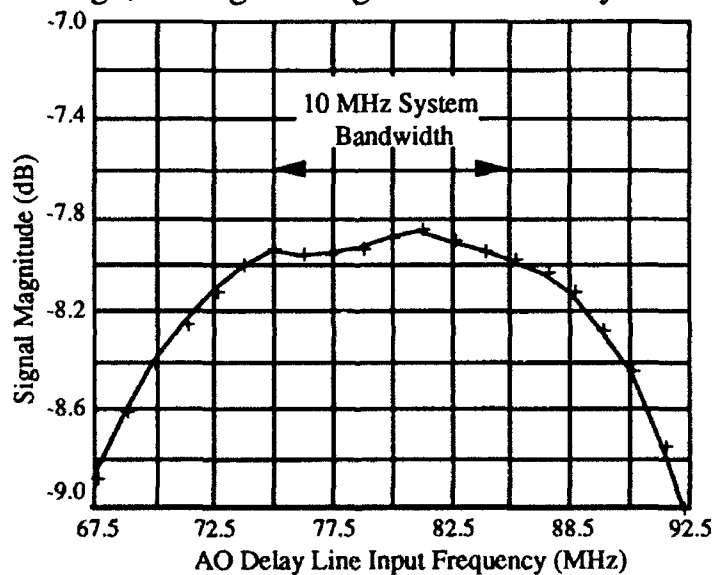


**Figure 4.2.2.b** Frequency Response at a Tap Position Corresponding to an AOSLM Input Frequency of 76 MHz<sup>22</sup>

Another test performed on the AO tapped delay line demonstrated the ability to cancel a pulsed signal using a single tap. The RF reference signal is split, with one replica being amplified to drive the AO delay line and the second replica fed into one input on an inverting ( $180^\circ$ ) summer (Mini-Circuits Model ZFSCJ-2-1). The AOSLM produces a single tap on the delay line and the photodiode collects the resultant delayed signal which in turn is fed into the second input of the inverting summer. The output of the summer is observed on an RF spectrum analyzer. The tap position and amplitude are tuned to minimize the signal level as measured by the spectrum analyzer.

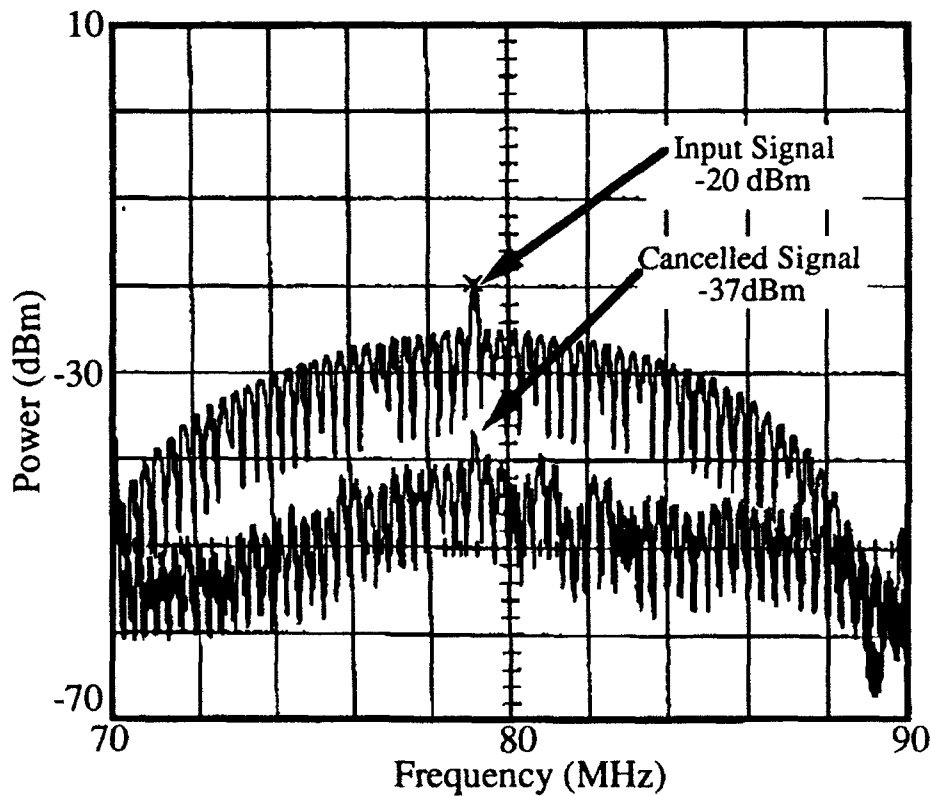


**Figure 4.2.2.c Cancellation of Pulsed RF Input (100 nsec pulse width, 3  $\mu$ sec repetition) With a Single Tap.**

Figure 4.2.2.c shows more than 15 dB cancellation for a 100 nsec pulse with 3  $\mu$ sec repetition, on an 80 MHz carrier. Figure 4.2.2.d shows almost 35 dB cancellation for a 500 nsec pulse with 3  $\mu$ sec repetition, on the 80 MHz carrier. The cancellation performance seems to improve with increasing pulsewidth.

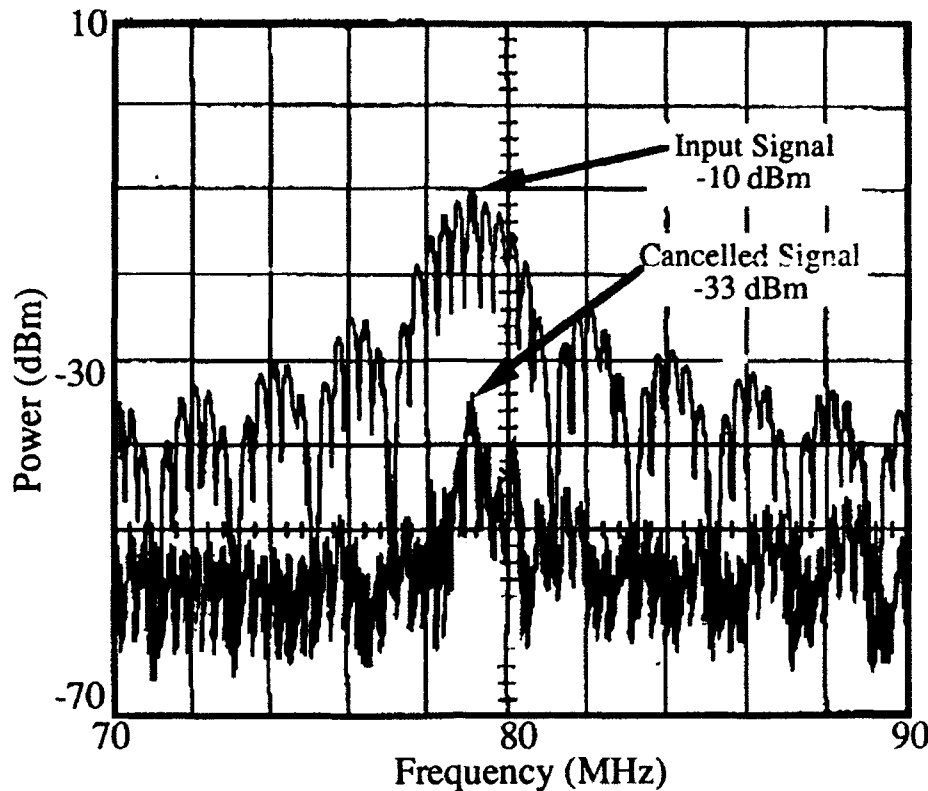


Figure 4.2.2.d Cancellation of Pulsed RF Input (500 nsec pulse width, 3  $\mu$ sec repetition) With a Single Tap.

### 4.3 CCD Cameras, Computer Interface, Controlling Software.

**4.3.1 Hardware Description.** The hardware required to collect the correlation information from the optical correlator and translate this result into taps on the optical delay line is depicted in Figure 4.3.1.a. The detectors used for the correlator are Reticon LC1901 linear charge-coupled photodiode arrays each with 512 pixels. The arrays are interfaced to a personal computer through a Girard 3197 8-bit A/D converter. This computer serves as the interface between the time-integrating correlator, described in Section 4.1, and the AO tapped delay line described in Section 4.2.

Some of the features gained through the software developed for this project include correlation display, computer control of various camera parameters (such as integration time), and control of various signal generation devices used to drive the AOSLM in the AO tapped delay line subsystem. An additional feature allows for the subtraction of background amplitude non-uniformities which appear in each of the two paths of the time-integrating correlator. Use of this last capability generates a low-noise signal for processing, improving the correlation results.



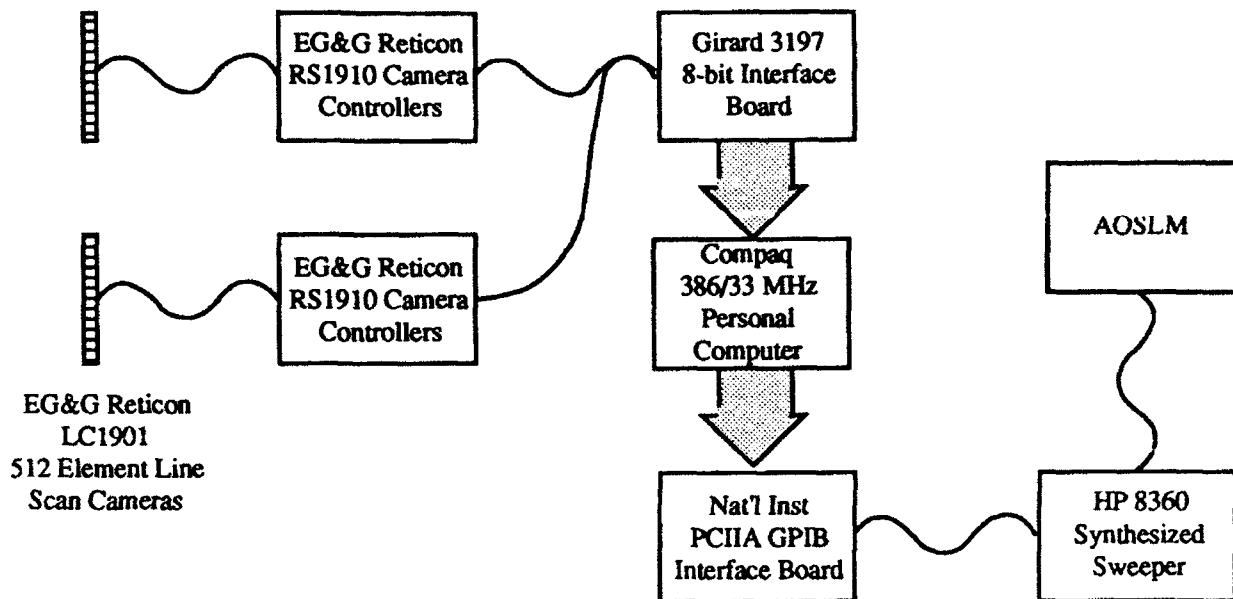


**Figure 4.3.1.a Computer Controlled Interface.** The line scan cameras collect the correlation data from the time integrating correlator. The interface shown here processes the correlation information and forms optical taps on an AO delay line via the AOSLM.

**4.3.2 Computer Software Description.** The software developed for this project allowed for near real time viewing of the correlation results. The hardware/software system retrieved raw correlation data from the CCD camera, cleaned and processed those data, and displayed the end product on the computer's monitor. This was accomplished at a rate of approximately four frames per second.

The signal cleaning involved two processes. The first was a background subtraction which eliminated many of the amplitude non-uniformities introduced by the optical system. The other cleaning process ensured that, for a given spatial carrier, the amplitude of each carrier peak was essentially constant across the aperture of the CCD array. These results were then to be extrapolated back to the signal of interest in the hopes of filtering out small scale non-uniformities that were causing erroneous results with the signal processing.

Other minor pre-processing measures included introducing a bias level (which was discounted for the actual signal processing), taking the absolute value of the signal (in order to get a better idea of the true nature of the envelope function), and an average subtraction (to ensure that the absolute value was being

taken around the average level of the cleansed signal).

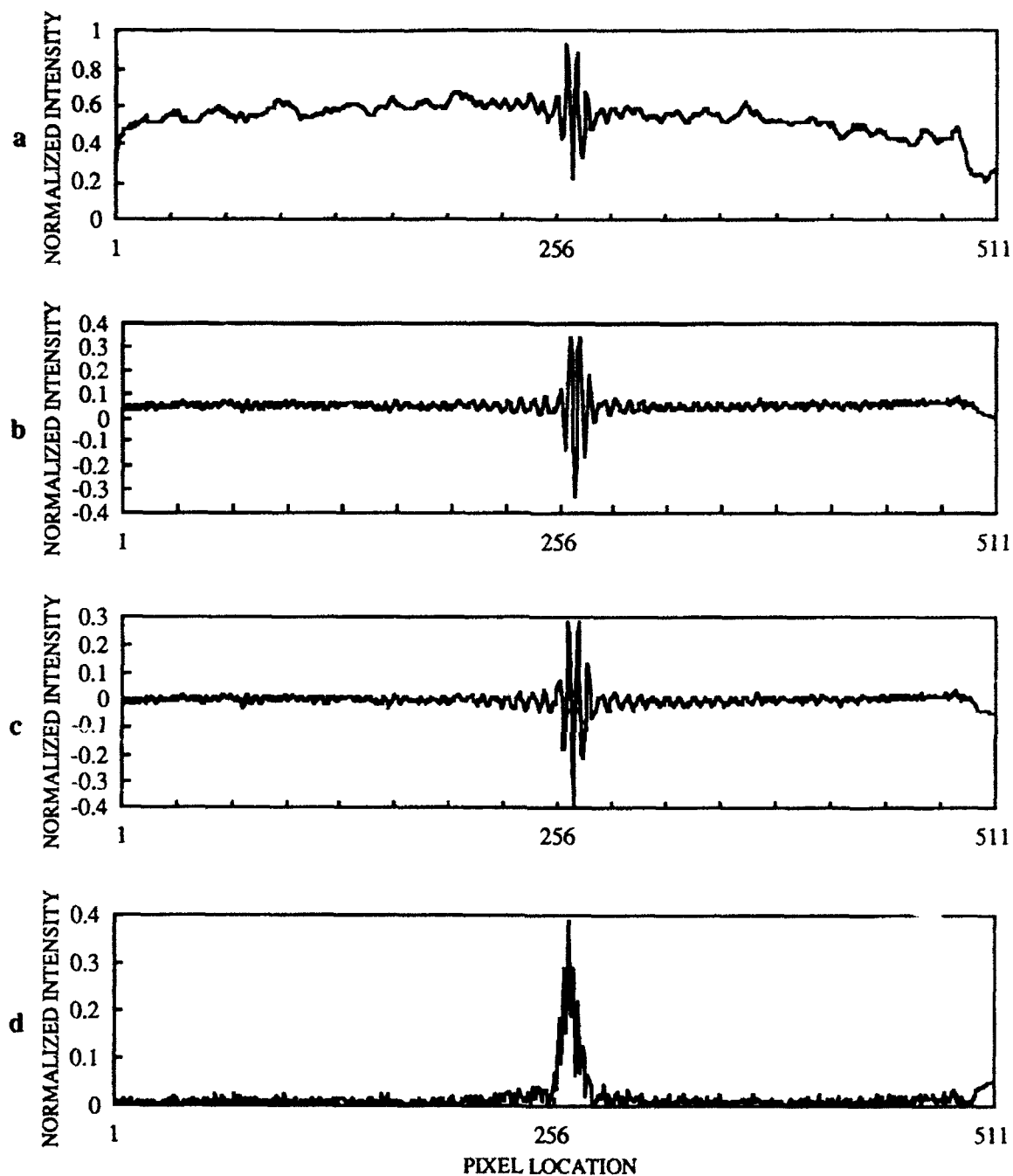
Once the signal was cleansed, the main signal processing could take place. This involved using one of two methods for determining the location of the correlation peak. The first method was a simple search for the highest value of the pre-processed signal. The other method was somewhat more sophisticated. It involved fitting the pre-processed data to a triangle and extrapolating the peak of the triangle. This was then used as the correlation peak of the system. During each iteration, peak picking results would be averaged with the previous  $n$  peaks. This induced stability of the resulting peak by reducing the amplitude of high frequency oscillations. Once the peak was selected for a particular iteration, a calibration factor was introduced and used from the input to a Hewlett-Packard 83623A Sweep Synthesizer via a GPIB interface. The amplified output of the synthesizer drove the AOSLM. Positional and amplitude information of the correlation peak corresponded to a drive frequency and amplitude (respectively) for the AOSLM.

### **4.3.3 Test Results for Software Based Signal Processing.**

**4.3.3.1 Software Pre-Processing.** Figures 4.3.3.1.a-g show the results of the successive pre-processing of the correlation results. Figure 4.3.3.1.a shows the raw data of an optically computed autocorrelation of a 10 MHz bandwidth noise signal collected by the CCD camera. Figure 4.3.3.1.b is the same image, adjusted for background non-uniformities. Figure 4.3.3.1.c resulted after subtracting the arithmetic mean of the data. Figure 4.3.3.1.d is the absolute value of Figure 4.3.3.1.c.

Figures 4.3.3.1.e-f show the results of removing the carrier non-uniformities. Figure 4.3.3.1.e is the raw data from the camera. The image is that of the spatial carrier with which the correlation is mixed. Figure 4.3.3.1.f shows the effect of normalizing the spatial carrier amplitude.

When the multiplicative factors derived from the data in Figure 4.3.3.1.e were used on the autocorrelation of a noise source on that spatial carrier, the results were somewhat disappointing. The power level in each of the Bragg cells was not constant between the calibration on the spatial carrier and the autocorrelation of the wide bandwidth noise. As such, the background non-uniformities for the Bragg cell were different for each of the two waveforms, and the correlation of the noise was distorted as shown in Figure 4.3.3.1.g.



**Figures 4.3.3.1.a-d. Preprocessing of Autocorrelation Data of 10 MHz Noise Source** (a) Raw data from CCD array . (b) Background amplitude non-uniformities subtracted. Note that the average value of all pixels is 0.05. (c) Background amplitude non-uniformities subtracted and average of all pixels values subtracted. (d) Absolute value of (c).

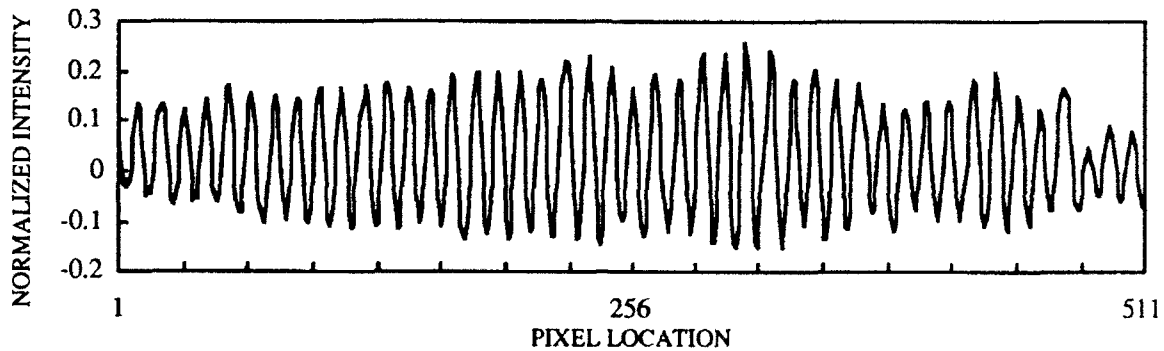


**Figure 4.3.3.1.e Spatial Carrier (Center Frequency=80 MHz) Prior to Amplitude Unification.**

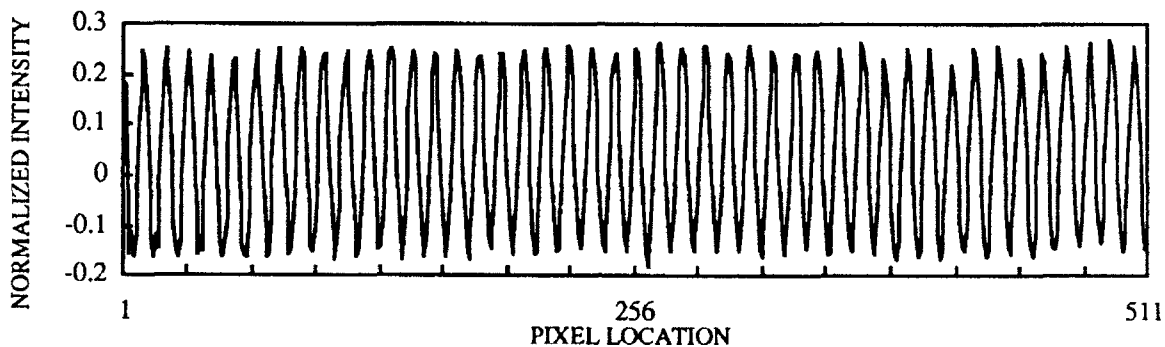


**Figure 4.3.3.1.f Spatial Carrier After Amplitude Unification.**

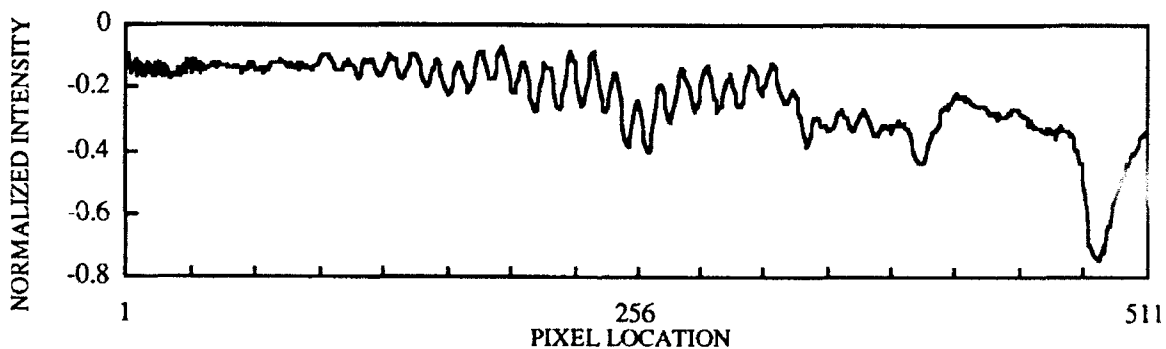


**Figure 4.3.3.1.g Effects of Spatial Carrier Unification on the Correlation of Wide Bandwidth Noise.**

**4.3.3.2 Correlation Peak Determination.** Two methods of correlation peak determination were used. The first was a simple search across the pre-processed correlation data for the maximum height. The other fit the preprocessed data to a triangle and determined its fit and triangle peak determination. Both peak determination methods produced cancellation results comparable to one another.

Due to highly sensitive alignment issues in the AO tapped delay line, small instabilities of the location of successive peaks would frequently cause the system to fall on and off the desired tap location. This was addressed by adding a filter to reduce the amplitude of these high frequency fluctuations.

A time window was selected and the location of the peak was averaged over that time window. In general, the larger the time window over which the averaging was performed, the greater the amplitude suppression of the high frequency fluctuations. Reasonable performance resulted when a window size of more than 40 frames was used. Thus, the running average spanned a time window of about 10 seconds. The resulting reduction in jammer signal strength fluctuated between 20 dB and 30 dB.

There are problems with this approach, however. Consider an environment in which the RF energy to be cancelled is changing rapidly. The averaging to smooth out high amplitude high frequency changes in the optical system will also filter out high frequency, high amplitude changes in the RF environment. If the environment is changing more rapidly than the filtered peak picking response time, the system will never be able to determine and hold an estimate of the proper tap characteristics.

**5.0 Conclusions and Recommendations.** The Multichannel Adaptive Optical Processor (MADOP) has been designed, and the three major subsystems (multichannel time integrating correlator, multichannel acousto-optic tapped delay line, and computer-based camera interface) have been fabricated. The optical systems have been constructed on two 2' x 3' optical breadboards for transportability. Initial test results demonstrate that each of these subsystems is capable of independent operation. This satisfies the major goals of Phase II of this program to develop an optical processor for adaptive jamming cancellation for the Rome Lab C-band antenna. Under Phase III, the goals are to fully characterize the MADOP as constructed, to make necessary upgrades to correct for system deficiencies, and to conduct laboratory and on-line testing of the completed system. At this point in the program, we identify the following challenges.

**5.1 Recommendations for Time Integrating Correlator.** The Mach-Zehnder Interferometric Time Integrating Correlator architecture is inherently vibration sensitive, especially to air currents. Currently, the subsystem has been placed in a sealed environment on a vibration isolation table due to this extreme sensitivity. This problem may be alleviated somewhat by cementing optics (especially beamsplitter BS2 in Figure 3.2.2. ) into their mounts and by providing additional mechanical support to the mirror mounts. Perhaps a

plexiglass enclosure could minimize the effect of air currents. We also recommend re-visiting the in-line architecture discussed in Section 3.2.1. This robust design would provide the needed stability and would reduce overall system complexity by eliminating the need for the fourth multichannel AO deflector. Riza<sup>39</sup> recommends a refinement of the architecture discussed in Section 3.2.1 which would make the subsystem even more optically efficient.

**5.2 Recommendations for Computer Interfaces** The digital/optical interface has a number of problems summarized below that should be addressed in future efforts if this system is going to lead to a general purpose method of noise cancellation.

1. The software is currently able to deal with fairly simple pulses and wide-band noise. It is, however, limited to picking only one correlation peak at a time. This will have to be dealt with if there are multiple delays of the signal in any of the channels.

2. The system currently has slow analog-to-digital and digital-to-analog conversion, owing largely to the speed limitations of the Girard 3197 and the GPIB interface boards. A substantial speed improvement can be realized if these boards are replaced with a faster (and more costly) data communications capability. The analog equipment would also have to be replaced with items that have the capability to communicate with those higher speed interfaces.

3. Additionally, the communications between the controller boards and the computer's CPU can be increased by switching to an EISA architecture bus. This will increase the speed of communications between the boards and the CPU by as much as four times. (Standard 16-bit ISA bus architectures are capable of data transfer rates of 8Mbits per second. The newer 32-bit EISA bus architecture are capable of transfer rates up to 33Mbits per second.) One means of significantly improving system speed would be to replace the existing Compaq DeskPro 386/33 with an EISA bus computer, the existing ISA A-D and D-A cards with EISA VME or special purpose interface cards, and the analog equipment that senses and controls the optical system with new equipment that operates with these interface cards.

The existing graphics capability on the Compaq Deskpro 386/33 is outdated and slow. Co-processed graphics boards exist which can increase the display speed by more than fifty times the existing capability. Further, these systems are fairly inexpensive when compared to the speed advantage they will offer and may do more to increase overall system speed than replacing the computer, the

converter cards, and the analog equipment.

4. As described in Section 4.3.3.2, high amplitude, high frequency fluctuations in the correlation peak lead to instabilities in the cancellation. The short term solution was basically a bubble-gum and bailing wire fix to the problem. The introduction of the multiple tap location capability presented by the planned programmable laser diode array, will eliminate the need to pick an individual peak. Further, more tap locations may lead to better overall performance of the system.

Additionally, the computer interface to the AOSLM is not yet well developed. A set of GPIB controllable frequency synthesizers could provide the driving signals for the AOSLM. Further study into replacing the computer with dedicated electronics is also recommended. We feel that if the MADOP is to be a viable technology for Air Force applications, then the camera-computer-AOSLM system should be replaced with a custom photodiode array-laser diode array circuit as discussed in Section 3.4.3, Reference 35, and shown in Figure 3.4.3.a.

**5.3 Recommendations for AO Tapped Delay Line.** The AOSLM is a cumbersome approach at best due to the limitations in the number of simultaneously addressed taps it can generate. However, at this time it is the only SLM technology available which provides continuously tunable and amplitude weighted tap positions. A major thrust in the Phase III effort will be to investigate alternatives to the AOSLM. The most likely candidate for replacing the AOSLM is a high-density laser diode array, such as that examined in Section 3.3.2.

**5.4 Concluding Remarks.** In conclusion, Phase II of the MADOP development resulted in the design and fabrication of the major subsystems. The emphasis of Phase III should first be placed on making the upgrades recommended above, on improving the interfaces between the subsystems, and on demonstrating successful closed-loop adaptive cancellation of laboratory test signals. The system will then be ready for on-line testing with the C-band antenna.

## 6.0 References

1. Ward, M.J., C.W. Keefer, S.T. Welstead, "Adaptive Optical Processor," Final In-House Report, RL-TR-91-270, (1991).
2. Blanchard, D.M., M.J. Ward, "Characterization of Liquid Crystal Displays for Optical Signal Processing Applications," In-House Report, RADC-TR-89-226, (1989).
3. Welstead, S.T., M.J. Ward, D.M. Blanchard, G.A. Brost, S.L. Halby, "Adaptive Signal Processing Using a Liquid Crystal Television," SPIE Proc., 1154, pp 244-252, (1989).
4. Ward, M.J., C.W. Keefer, D.J. Gruzca, S.T. Welstead, "Comparison of Spatial Light Modulators for Multipath Delay Estimation," OSA Technical Digest, 14, pp 149-152, (1990).
5. Ward, M.J., C.W. Keefer, S.T. Welstead, "Spatial Light Modulation Techniques for System Application to Multipath Delay Estimation", Appl Opt., 31, pp 4010-4015 (1992).
6. Welstead, S.T., M.J. Ward, "Extended Dynamic Range One Dimensional Spatial Light Modulator," U.S. Patent 5039210, (1991).
7. Welstead, S.T., M.J. Ward, "Hybrid Electro-Optic Processor," Final Report for contract F30602-88-D-0028, RL-TR-91-164, (1991).
8. Welstead, S.T., "Optical Processor Evaluation," Final Report for contract F30602-88-D-0028, RL-TR-91-34, (1991).
9. Welstead, S.T., M.J. Ward, C.W. Keefer, "Neural Network Approach to Multipath Delay Estimation," SPIE Proc., 1565, pp 482-495, (1991).
10. Welstead, S.T., "Algorithms for Multichannel Optical Processor," Final Report for contract F30602-88-D-0028, RL-TR-92-78, (1992).
11. Budge, M.C., R.G. Berinato, M.C. Zari, "Acousto-Optic Applications for Multichannel Optical Processor," Final Report for contract F30602-91-D-0001, RL-TR-92-160, (1992).
12. Budge, M.C., R.G. Berinato, M.C. Zari, "Alternative Acousto-Optic



Architectures for Multichannel Optical Processor," Final Report for contract F30602-92-C-0026, in preparation, (1993).

13. Widrow, B., S.D. Stearns, Adaptive Signal Processing, Prentice-Hall, Inc., Englewood Cliffs, NJ, (1985).

14. Sprague, R.A., C.L. Koliopoulos, "Time Integrating Acoustooptic Correlator," Appl Opt, **15**, pp 89-92, (1976).

15. Kellman, P., "Time Integrating Optical Signal Processor," Dissertation, Stanford University, Stanford, CA, (1979).

16. Rotz, F.B., "Time Integrating Optical Correlator," SPIE Proc., **202**, pp 163-169, (1979).

17. Abramovitz, J.J., N.J. Berg, M.W. Casseday, "Coherent Time Integration Processors," in Acousto-Optic Signal Processing, ed. N.J. Berg and J.N. Lee, Marcel-Dekker, Inc., New York, pp 289-323, (1983).

18. VanderLugt, A., Optical Signal Processing, John Wiley & Sons, Inc., New York, pp 504-530.

19. VanderLugt, *ibid*, p 369ff, and p. 504ff.

20. Zari, M.C., R.G. Berinato, M.J. Ward, H.G Andrews II, "Multichannel Optical Time Integrating Correlator for Adaptive Jamming Cancellation," SPIE Proc., **1703**, pp 88-97, (1992).

21. Freyer, F.W., "Continuously Variable Delay Line," U.S. Patent 4390247, (1983).

22. Berinato, R.J., "Acousto-Optic Tapped Delay Line," submitted for future publication in Appl Opt.

23. Keefer, C.W., M.J. Ward, D.J. Grucza, "Acousto-Optic Programmable Delay Line Using Laser Diodes", SPIE Proc., **1790**, to be published, (1992).

24. Whitman, R.L., A. Korpel, "Probing of Acoustic Surface Perturbations by Coherent Light," Appl Opt, **8**, pp 1567-1576, (1969).

25. VanderLugt, *ibid*, pp 374-378.

26. Penn, W.A., "Acousto-Optic Adaptive Processor (AOAP) - Phase II," Final Report for contract F30602-81-C-0264, RADC-TR-86-188, (1986).
27. Penn, W.A., R. Wasiewicz, R.M. Iodice, "Optical Adaptive Multipath Canceler for Surveillance Radar," SPIE Proc., **1217**, pp 151-160, (1990).
28. Friedman, D.B., "Design Requirements Development for a Penn-Dickey Acousto-Optic Adaptive Processor," SPIE Proc., **1703**, to be published, (1992).
29. Montgomery, R.M., "Acousto-Optic/Photorefractive Processor for Adaptive Antenna Arrays," SPIE Proc., **1217**, pp 207-217, (1990).
30. Montgomery, R.M., M.R. Lange, "Photorefractive Adaptive Filter Structure with 40-dB Interference Rejection," *Appl Opt*, **30**, pp 2844-2849, (1991).
31. Montgomery, R.M., W.B. Beaudet, M.R. Lange, "Photorefractive Adaptive Sidelobe Canceler for Phased Array Antennas," SPIE Proc., **1217**, pp 207-217 (1990).
32. Wasiewicz, R., R.M. Iodice, W.A. Penn, D.B. Friedman, "Acousto-Optic Adaptive Processor (AOAP) Enhancements," Final Report for contract F30602-88-C-0141, RL-TR-92-13, (1992).
33. Keefer, C.W., J.E. Malowicki, P.M. Payson, "Modified Acousto-Optic Adaptive Processor," Final In-House Report, in preparation.
34. Vacchs, F., J.H. Hong, C.W. Keefer, "Operation of an Adaptive Processor Using a Photorefractive Parallel Integrator," SPIE Proc., **1703**, to be published, (1992).
35. Keefer, C.W., J.E. Malowicki, P.M. Payson, "Wideband Operation of a Photorefractive Based Adaptive Processor," SPIE Proc., **1790**, to be published, (1992).
36. Brost, G.A., C.W. Keefer, "Alternating Electric Field Frequency Influence on Photorefractive Characteristics," OSA Annual Meeting, Albuquerque, NM, September, (1992).
37. VanderLugt, *ibid*, pp 146-152.

38. Conversation with R.M. Montgomery at Rome Laboratory, Griffiss AFB, NY, March, 1992.

39. Riza, N.A., "Optically Efficient Interferometric Acousto-optic Architecture for Spectrum Analysis," Appl Opt, 31, pp 3194-3196, (1992).